

Search for topological defect dark matter using the global network of optical magnetometers for exotic physics searches (GNOME)

Samer Afach

Johannes Gutenberg-Universität

Ben Buchler

Australian National University <https://orcid.org/0000-0002-2852-7483>

Dmitry Budker

University of California at Berkeley <https://orcid.org/0000-0002-7356-4814>

Conner Dailey

University of Nevada <https://orcid.org/0000-0003-2488-3461>

Andrei Derevianko

University of Nevada Reno <https://orcid.org/0000-0002-7105-4853>

Vincent Dumont

Lawrence Berkeley National Laboratory

Nataniel L. Figueroa

Johannes Gutenberg-Universität Mainz

Ilja Gerhardt

University of Stuttgart

Zoran Grujic

University of Belgrade

Hong Guo

Peking University

Chuanpeng Hao

University of Science and Technology of China

Paul Hamilton

University of California

Morgan Hedges

The Australian National University

Derek Jackson Kimball

California State University – East Bay <https://orcid.org/0000-0003-2479-6034>

Dongok Kim

Korea Advanced Institute of Science and Technology <https://orcid.org/0000-0002-4097-2889>

Sami Khamis

University of California

Thomas Kornack

Twinleaf LLC

Victor Lebedev

University of Fribourg

Zheng-Tian Lu

University of Science and Technology of China

Hector Masia-Roig (✉ hemasiar@uni-mainz.de)

Johannes Gutenberg-Universität

Madeline Monroy

University of California - Berkeley

Mikhail Padniuk

Jagiellonian University in Krakow <https://orcid.org/0000-0002-8709-143X>

Christopher Palm

California State University – East Bay

Sun Yool Park

JILA, NIST and University of Colorado Boulder

Karun Paul

The Australian National University

Alexander Penafior

California State University – East Bay

Xiang Peng

Peking University

Maxim Pospelov

University of Minnesota

Rayshaun Preston

California State University – East Bay

Szymon Pustelny

Jagiellonian University in Krakow

Theo Scholtes

Leibniz Institute of Photonic Technology

Perrin Segura

Harvard University

Yannis Semertzidis

Institute for Basic Science <https://orcid.org/0000-0001-7941-6639>

Dong Sheng

University of Science and Technology of China

Yun Chang Shin

Institute for Basic Science

Joseph Smiga

Johannes Gutenberg-Universität Mainz <https://orcid.org/0000-0002-5492-5485>

Jason Stalnaker

Oberlin College

Ibrahim Sulai

Bucknell University

Dhruv Tandon

Oberlin College

Tao Wang

Princeton University

Antoine Weis

University of Fribourg

Arne Wickenbrock

Johannes Gutenberg-Universität Mainz

Tatum Wilson

California State University – East Bay

Teng Wu

Peking University

David Wurm

Technische Universität München <https://orcid.org/0000-0003-1287-7427>

Wei Xiao

Peking University

Yucheng Yang

Peking University <https://orcid.org/0000-0003-4568-3450>

Dongrui Yu

Peking University

Jianwei Zhang

Peking University

Article

Keywords: Transient Signals, Exotic Fields, Earth-scale Detector, Ultralight Bosons, Axion-like Particles, Dark Matter Scenarios,

Posted Date: April 7th, 2021

DOI: <https://doi.org/10.21203/rs.3.rs-298059/v1>

License:  This work is licensed under a Creative Commons Attribution 4.0 International License.

[Read Full License](#)

Version of Record: A version of this preprint was published at Nature Physics on December 7th, 2021. See the published version at <https://doi.org/10.1038/s41567-021-01393-y>.

Search for topological defect dark matter using the global network of optical magnetometers for exotic physics searches (GNOME)

Samer Afach,^{1,2} Ben C. Buchler,³ Dmitry Budker,^{1,2,4} Conner Dailey,^{5,*} Andrei Derevianko,⁵ Vincent Dumont,⁶ Nataniel L. Figueroa,^{1,2} Ilja Gerhardt,⁷ Zoran D. Grujić,^{8,9} Hong Guo,¹⁰ Chuanpeng Hao,¹¹ Paul S. Hamilton,¹² Morgan Hedges,³ Derek F. Jackson Kimball,¹³ Dongok Kim,^{14,15} Sami Khamis,¹² Thomas Kornack,¹⁶ Victor Lebedev,⁹ Zheng-Tian Lu,¹⁷ Hector Masia-Roig,^{1,2,†} Madeline Monroy,^{4,13} Mikhail Padniuk,¹⁸ Christopher A. Palm,¹³ Sun Yool Park,^{19,‡} Karun V. Paul,³ Alexander Penaflo,¹³ Xiang Peng,¹⁰ Maxim Pospelov,^{20,21} Rayshaun Preston,¹³ Szymon Pustelny,¹⁸ Theo Scholtes,^{9,22} Perrin C. Segura,^{19,§} Yannis K. Semertzidis,^{14,15} Dong Sheng,¹¹ Yun Chang Shin,¹⁴ Joseph A. Smiga,^{1,2,¶} Jason E. Stalnaker,¹⁹ Ibrahim Sulai,²³ Dhruv Tandon,¹⁹ Tao Wang,²⁴ Antoine Weis,⁹ Arne Wickenbrock,^{1,2} Tatum Wilson,¹³ Teng Wu,¹⁰ David Wurm,²⁵ Wei Xiao,¹⁰ Yucheng Yang,¹⁰ Dongrui Yu,¹⁰ and Jianwei Zhang¹⁰

¹*Johannes Gutenberg-Universität Mainz, 55128 Mainz, Germany*

²*Helmholtz-Institut Mainz, GSI Helmholtzzentrum für Schwerionenforschung, 55128 Mainz, Germany*

³*Centre for Quantum Computation and Communication Technology,*

Research School of Physics, The Australian National University, Acton 2601, Australia

⁴*Department of Physics, University of California at Berkeley, Berkeley, California 94720-7300, USA*

⁵*Department of Physics, University of Nevada, Reno, Nevada 89557, USA*

⁶*Computational Research Division, Lawrence Berkeley National Laboratory, Berkeley, CA 94720, USA*

⁷*Institute for Quantum Science and Technology (IQST), 3rd Institute of Physics, and Max Planck Institute for Solid State Research, D-70569 Stuttgart, Germany*

⁸*Institute of Physics Belgrade, University of Belgrade, 11080 Belgrade, Serbia*

⁹*Physics Department, University of Fribourg, Chemin du Musée 3, CH-1700 Fribourg, Switzerland*

¹⁰*State Key Laboratory of Advanced Optical Communication Systems and Networks, Department of Electronics, and Center for Quantum Information Technology, Peking University, Beijing 100871, China*

¹¹*Department of Precision Machinery and Precision Instrumentation,*

University of Science and Technology of China, Hefei 230026, P. R. China

¹²*Department of Physics and Astronomy, University of California, Los Angeles, California 90095, USA*

¹³*Department of Physics, California State University – East Bay, Hayward, California 94542-3084, USA*

¹⁴*Center for Axion and Precision Physics Research, IBS, Daejeon 34051, Republic of Korea*

¹⁵*Department of Physics, KAIST, Daejeon 34141, Republic of Korea*

¹⁶*Twinleaf LLC, 300 Deer Creek Drive, Plainsboro, NJ 08536, USA*

¹⁷*Hefei National Laboratory for Physical Sciences at the Microscale,*

University of Science and Technology of China, Hefei 230026, P. R. China

¹⁸*Institute of Physics, Jagiellonian University in Krakow,*

prof. Stanisława Łojasiewicza 11, 30-348, Kraków, Poland

¹⁹*Department of Physics and Astronomy, Oberlin College, Oberlin, OH 44074, USA*

²⁰*School of Physics and Astronomy, University of Minnesota, Minneapolis, MN 55455, USA*

²¹*William I. Fine Theoretical Physics Institute, School of Physics and Astronomy,*

University of Minnesota, Minneapolis, MN 55455, USA

²²*Leibniz Institute of Photonic Technology, Albert-Einstein-Straße 9, D-07745 Jena, Germany*

²³*Department of Physics and Astronomy, One Dent Drive,*

Bucknell University, Lewisburg, Pennsylvania 17837, USA

²⁴*Department of Physics, Princeton University, Princeton, New Jersey, 08544, USA*

²⁵*Technische Universität München, 85748 Garching, Germany*

(Dated: February 26, 2021)

Results are reported from the first full-scale search for transient signals from exotic fields of astrophysical origin using data from a newly constructed Earth-scale detector: the Global Network of Optical Magnetometers for Exotic physics searches (GNOME). Data collected by the GNOME consist of correlated measurements from optical atomic magnetometers located in laboratories all over the world. GNOME data are searched for patterns of signals propagating through the network consistent with exotic fields composed of ultralight bosons such as axion-like particles (ALPs). Analysis of data from a continuous month-long operation of the GNOME finds no statistically significant signals consistent with those expected due to encounters with topological defects (axion domain walls), placing new experimental constraints on such dark matter scenarios.

I. INTRODUCTION

The nature of dark matter, an invisible substance comprising over 80% of the mass of the universe [1–3], is one of the most profound mysteries of modern physics. Although evidence for the existence of dark matter comes from its gravitational interactions, unraveling its nature likely requires observing non-gravitational interactions between dark matter and ordinary matter [4]. One of the leading hypotheses is that dark matter consists of ultralight bosons such as axions [5–7] or axion-like particles (ALPs) [8–10]. Axions and ALPs arise from spontaneous symmetry breaking at an unknown energy scale f_{SB} , which, along with their mass m_a , determines many of their physical properties.

ALPs can form stable, macroscopic field configurations in the form of topological defects [11–14] or composite objects bound together by self-interactions such as boson stars [15–17]. Such ALP field configurations could concentrate the dark matter density into many distinct, compact spatial regions that are small compared to the galaxy but much larger than the Earth. In such scenarios, Earth-bound detectors would only be able to measure signals associated with dark matter interactions on occasions when the Earth passes through such a dark-matter object. It turns out that there is a wide range of parameter space, consistent with observations, for which such dark-matter objects can have the required size and abundance such that the characteristic time between encounters could be on the order of one year or less [13, 17, 18]. This opens up the possibility of searches with terrestrial detectors. Here we present the results of such a search for ALP domain walls, a class of topological defects which can form between regions of space with different vacua of an ALP field [11–14].¹

Since ALPs can interact with atomic spins [4], the passage of Earth through an ALP domain wall affects atomic spins similarly to a transient magnetic field pulse [13, 17]. Considering a linear coupling between the ALP field gradient $\nabla a(\mathbf{r}, t)$ and atomic spin \mathbf{S} , the interaction Hamil-

tonian can be written as

$$H_{\text{lin}} = -(\hbar c)^{3/2} \frac{\xi}{f_{\text{SB}}} \frac{\mathbf{S}}{\|\mathbf{S}\|} \cdot \nabla a(\mathbf{r}, t), \quad (1)$$

where \hbar is the reduced Planck’s constant, c is the speed of light, \mathbf{r} is the position of the spin, t is the time, and $f_{\text{SB}}/\xi \equiv f_{\text{int}}$ is the coupling constant in units of energy described with respect to the symmetry-breaking scale f_{SB} [21], where ξ is unitless. In most theories, the coupling constants f_{int} describing the interaction between Standard Model fermions and the ALP field are proportional to f_{SB} ; however, f_{int} can differ between electrons, neutrons, and protons by model-dependent factors that can be significant in some cases [4, 8].

In analogy with Eq. (1), the Zeeman Hamiltonian describing the interaction of a magnetic field \mathbf{B} with an atomic spin \mathbf{S} can be written as

$$H_Z = -\gamma \mathbf{S} \cdot \mathbf{B}, \quad (2)$$

where γ is the gyromagnetic ratio. Since Eqs. (1) and (2) have the same structure, the gradient of the ALP field can be treated as a pseudo-magnetic field. An important distinction between the ALP-spin interaction [Eq. (1)] and the Zeeman interaction [Eq. (2)] is that while γ tends to scale inversely with the fermion mass, no such scaling of the ALP-spin interaction is expected [4].

The amplitude, direction, and duration of the pseudo-magnetic field pulse associated with the transit of the Earth through an ALP domain wall depends on many unknown parameters such as the energy density stored in the ALP field, the coupling constant f_{int} , the thickness of the domain wall, and the relative velocity \mathbf{v} between Earth and the domain wall. The dynamical parameters, such as the velocities of the dark matter objects, are expected to randomly vary from encounter-to-encounter. We assume that they are described by the Standard Halo Model for virialized dark matter [22]. Furthermore, the abundance of domain walls in the galaxy is limited by physical constants, m_a and f_{SB} , as these determine the energy contained in the wall and the total energy of all domain walls is constrained by estimates of the local dark matter density [23]. The expected temporal form of the pseudo-magnetic field pulse can depend both on the theoretical model describing the ALP domain wall as well as particular details of the terrestrial encounter such as the orientation of the Earth. The relationships between these parameters and characteristics of the pseudo-magnetic field pulses searched for in our analysis are discussed in Appendix A and Refs. [13, 17, 21].

The Global Network of Optical Magnetometers for Exotic physics searches (GNOME) is a worldwide network searching for correlated signals heralding beyond-the-Standard-Model physics which currently consists of more than a dozen optical atomic magnetometers, with stations in Europe, North America, Asia, the Middle East, and Australia. A schematic of a domain-wall encounter with the GNOME with stations used in this study is

* Currently: University of Waterloo, Department of Physics and Astronomy, N2L 3G1, Ontario, CA

† hemasiar@uni-mainz.de

‡ Currently: JILA, NIST and University of Colorado, and Department of Physics, University of Colorado, Boulder Colorado 80309-0440, USA

§ Currently: Department of Physics, Harvard University, Cambridge, MA 02138

¶ jsmiga@uni-mainz.de

¹ A different type of bosonic field configuration is the Q-ball [19, 20] which is spherically symmetric having nearly constant field magnitude in the bulk with a rapid fall off at the boundaries. It is another possible dark matter candidate. We note that the signal pattern produced in GNOME for sufficiently large Q-balls with couplings to atomic spins can be similar to that of ALP domain walls [17].

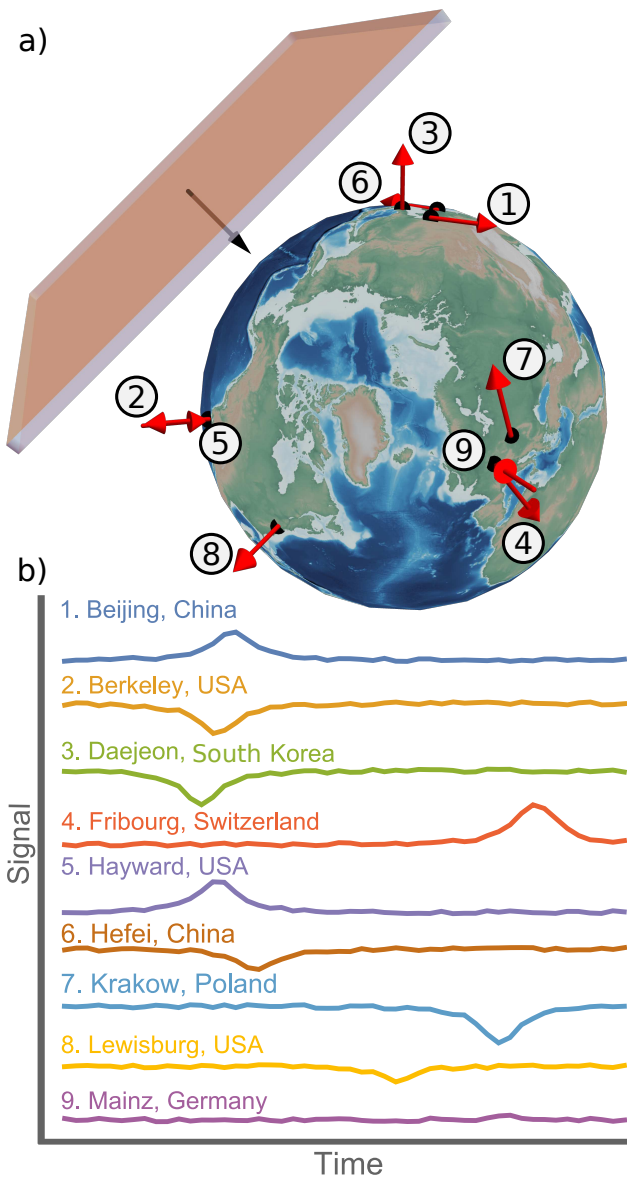


Figure 1. (a) Visualization of an ALP domain wall crossing the Earth. The red arrows indicate the position and sensitive axes of the GNOME magnetometers during Science Run 2 (Sec. I). (b) Simulation of the signals expected to be observed from a domain-wall crossing.

137 shown in Fig. 1. The measurements from the magne-
 138 tometers are recorded with data-acquisition systems, syn-
 139 chronized to the Global Positioning System (GPS) time,
 140 and uploaded to servers located in Mainz, Germany, and
 141 Daejeon, South Korea. Descriptions of the operational
 142 principles and characteristics of GNOME magnetome-
 143 ters are presented in Sec. IV and Ref. [24], details on
 144 the GNOME data acquisition system are discussed in
 145 Ref. [25] (see also Table I).

146 The active field sensor at the heart of every GNOME
 147 magnetometer is an optically pumped and probed gas
 148 of alkali atoms. Magnetic fields are measured through

149 variations in the Larmor spin precession of the optically
 150 polarized atoms. The vapor cells containing the alkali
 151 atoms are placed inside multi-layer magnetic shielding
 152 systems which reduce background magnetic noise by or-
 153 ders of magnitude [26] while retaining sensitivity to ex-
 154 otic spin-couplings between ALP dark matter and atomic
 155 nuclei.² Since all GNOME magnetometers presently use
 156 atoms whose nuclei have a valence proton, the signal am-
 157 plitudes measured by the GNOME due to an ALP-spin
 158 interaction are proportional to the relative contribution
 159 of the proton spin to the nuclear spin (as discussed in
 160 Appendix B and Ref. [28]). This pattern of signal ampli-
 161 tudes [Eq. (1)] can be characterized by a pseudo-magnetic
 162 field B_j measured with sensor j :

$$B_j = \frac{\sigma_j \eta_j}{g_{F,j}} \mathcal{B}_p, \quad (3)$$

163 where

$$\mathcal{B}_p(\mathbf{r}, t) = (\hbar c)^{3/2} \frac{2\xi}{\mu_B f_{SB}} \nabla a(\mathbf{r}, t) \quad (4)$$

164 is the normalized pseudo-magnetic field describing the
 165 effect of the ALP domain wall on proton spins and μ_B
 166 is the Bohr magneton. The ratio between the Landé g-
 167 factor and the effective proton spin ($g_{F,j}/\sigma_j$) accounts for
 168 the specific proton-spin coupling in the respective sensor.
 169 This ratio depends on the atomic and nuclear structure
 170 as well as details of the magnetometry scheme, see Ap-
 171 pendix B. Since each GNOME magnetometer measures
 172 the projection of the field along a particular sensitive
 173 axis, the factor η_j is introduced to account for the direc-
 174 tional sensitivity. This factor, given by the cosine of the
 175 angle between \mathcal{B}_p and the sensitive axes, takes on values
 176 between ± 1 .

177 In spite of the unknown properties of a particular
 178 terrestrial encounter with an ALP domain wall, the
 179 GNOME would measure a recognizable global pattern
 180 of the associated pseudo-magnetic field pulse amplitudes
 181 described by Eq. (3), as illustrated in Fig. 1b. The as-
 182 sociated pseudo-magnetic field pulses would point along
 183 a common axis, have the same duration, and exhibit a
 184 characteristic timing pattern. The data-analysis algo-
 185 rithm used in the present work to search for ALP domain
 186 walls is described in Sec. IV and Ref. [29]. The algo-
 187 rithm searches for a characteristic signal pattern across
 188 the GNOME having properties consistent with passage
 189 of the Earth through an ALP domain wall. Separate
 190 analyses to search for transient oscillatory signals associ-
 191 ated with boson stars [17] and bursts of exotic low-mass
 192 fields (ELFs) from cataclysmic astrophysical events [30]
 193 are presently underway.

194 Here we report the first results of a dark matter search
 195 with the GNOME: a search for transient couplings of

² Signals due to ALP interactions with electron spins can be coun-
 teracted by effects from interaction between the ALP field and
 electron spins in the magnetic shielding material [27].

atomic spins to macroscopic dark-matter objects, and therefore demonstrate the ability of the GNOME to explore parameter space previously unconstrained by direct laboratory experiments. Searches for macroscopic dark-matter objects based on similar ideas were carried out using atomic clock networks [18, 31–33], and there are a number of experimental proposals utilizing other sensor networks [34–38]. All of these networks are sensitive to bosonic dark matter with a scalar coupling to Standard Model particles [4]. The GNOME is sensitive to a different class of dark matter: bosons with pseudoscalar couplings to Standard Model particles. Pseudoscalar bosonic dark matter generally produces no observable effects in clock networks [4] but does couple to atomic spins via the interaction described by Eq. (1). Thus the GNOME is sensitive to a distinct, so far mostly unconstrained, class of interactions as compared to other sensor networks.

II. RESULTS

There have been four GNOME Science Runs between 2017 and 2020 as discussed in Sec. IV. Here we analyze the data from Science Run 2, which had comparatively good overall noise characteristics and consistent network operation (as seen in Fig. 5). Nine magnetometers took part in Science Run 2 that spanned from 29 November 2017 to 22 December 2017. The characteristics of the magnetometers are summarized in Table I.

Before the data are searched for evidence of domain-wall signatures, they are preprocessed by applying a rolling average, high-pass filters, and notch filters to the raw data. The averaging enhances the signal-to-noise ratio for certain pulse durations, avoids complications arising from different magnetometers having different bandwidths, and reduces the amount of data to be analyzed. The high-pass and notch filters reduce the effects of long-term drifts and noisy frequency bands. We refer to the filtered and rolling-averaged data set as the “search data.”

The search data are examined for evidence of collective signal patterns corresponding to planes with uniform, non-zero thickness, crossing Earth at constant velocities. The imprinted pattern of amplitudes depends on the domain-wall crossing velocity [29]. As noted in Sec. I, we assume that the domain-wall-velocity probability density function follows the Standard Halo Model for virialized dark matter. The signature of a domain-wall crossing the magnetometer network depends on the perpendicular component to the domain-wall plane of the relative velocity between the Earth and the domain wall, v_{\perp} . A lattice of points in velocity space is constructed such that the search algorithm covers 97.5% of the velocity probability density function. The algorithm scans over the velocity lattice and, for every velocity, the data from each magnetometer are appropriately time-shifted so that the signals in different magnetometers from a hypothetical domain-wall crossing with the given velocity occur at the same time. For each velocity and at each measurement

time, the amplitudes measured by each magnetometer are fit to the ALP domain-wall crossing model described in Ref. [29]. As a result, estimations for signal magnitude and domain-wall direction, along with associated uncertainties, are obtained for each measurement time and all lattice velocities. The magnitude-to-uncertainty ratio of an event is given by the ratio between the signal magnitude and its associated uncertainty.

The search algorithm uses two different tests to evaluate if a given event is likely to have been produced by an ALP domain-wall-crossing: a domain-wall model test and a directional-consistency test [29]. The domain-wall model test evaluates whether the event amplitudes measured by the GNOME magnetometers match the signal amplitudes predicted by the ALP domain-wall crossing model, and is quantified by the p -value as discussed in Sec. IV and Ref. [29]. The directional-consistency test checks the agreement between the direction of the scanned velocity and the estimated domain wall direction, and is quantified by the angle between the two directions normalized by the angle between adjacent lattice velocities.

In order to evaluate the detection probability of the search algorithm, a well-characterized data set that includes domain-wall-crossing signals with known properties is required. For this purpose, we generate a background data set by randomly time-shuffling the search data so that the relative timing of measurements from different GNOME stations is shifted by amounts so large that no true-positive events could occur. By repeating the process of time shuffling, the length of the background data can be made to far exceed the search data. This method is used to generate background data with noise characteristics closely reproducing those of the search data [39]. A set of pseudo-magnetic field pulses matching the expected amplitude and timing pattern produced by the passages of Earth through ALP domain walls are inserted into the background data to create the test data. The test data are used to evaluate the true-positive probability for the search algorithm for different thresholds on the p -value and the normalized angular difference. The detection probability as a function of the thresholds is studied in order to find a combination of thresholds that ensures the detection of 97.5% of the inserted domain walls (see Sec. IV and Fig. 6). This results in an overall detection efficiency $\epsilon \geq 95\%$ for the search algorithm, considering both the incomplete velocity lattice coverage and the detection probability.

The search data are analyzed for domain-wall encounters using the algorithm presented in Ref. [29]. The cumulative distribution of candidate events as a function of their magnitude-to-uncertainty ratio is shown as a solid green line in Fig. 2. The background data are analyzed in the same way as the search data to estimate the expected number of background events during Science Run 2. Time-shuffling is used to create 10.7 years of background data. The number of candidate events measured in the background data re-scaled to the dura-

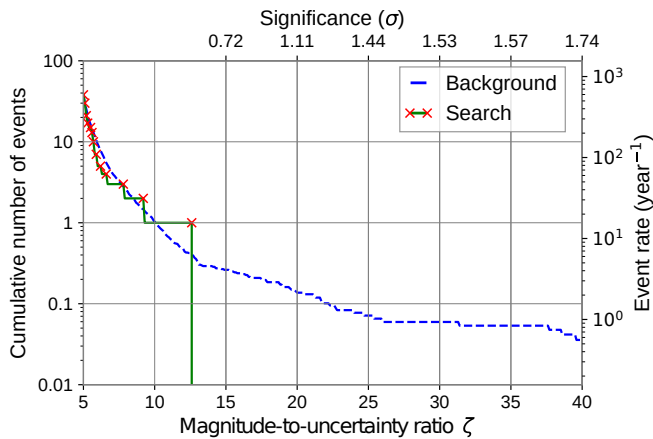


Figure 2. The blue dashed line represents the number events expected from the background in the twenty-three days of data from Science Run 2. 10.7 years of time-shuffled data are used to evaluate the background. The solid green line represents the number of events measured in Science Run 2. The red crosses indicate at which magnitude-to-uncertainty ratio new events are found. The upper axis indicates the statistical significance in units of Gaussian standard deviations of finding one event in the search data. The event with greatest magnitude-to-uncertainty ratio is found at 12.6.

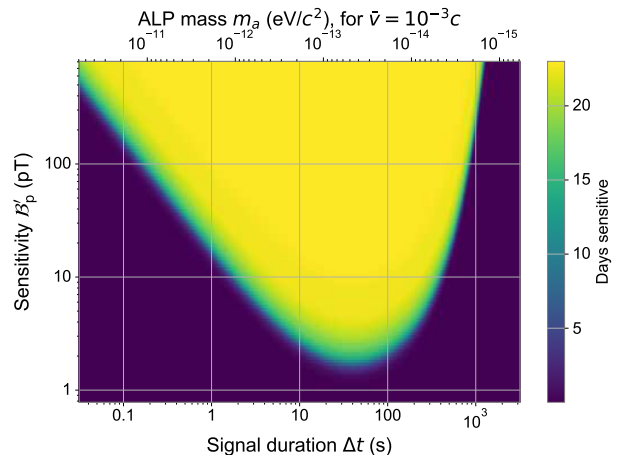


Figure 3. Amount of time \tilde{T} that the GNOME is sensitive to domain walls with a given duration Δt and normalized pseudo-magnetic field magnitude sensitivity \mathcal{B}'_p throughout Science Run 2, the magnitude of an event needed to induce a signal with a magnitude-to-uncertainty ratio of one [see Eq. (11)]. Only the worst-case direction is considered. The plot assumes the parameters of the analysis: 20s averaging time, 1.67 mHz first-order zero-phase Butterworth filter, and 50 Hz and 60 Hz zero-phase notch filters with a Q -factor of 60.

tion of Science Run 2 is shown as a dashed blue line in Fig. 2. The significance of a candidate event in the search data is given by the probability of detecting one or more background events at a magnitude-to-uncertainty ratio above that of the candidate event [see Eq. (10)]. The probability of finding a number of candidate events in the background data follows Poisson statistics.

The candidate event in the search data with the largest magnitude-to-uncertainty ratio ($= 12.6$) had a significance of less than one sigma. Therefore, we find no evidence of an ALP domain-wall crossing during Science Run 2.

In order to evaluate the domain-wall characteristics excluded by this result, the observable domain-wall crossing parameters above 12.6 magnitude-to-uncertainty ratio during Science Run 2 are determined. The GNOME has nonuniform directional sensitivity [29]; we conservatively estimate the network sensitivity assuming the domain wall comes from the least-sensitive direction. Figure 3 shows the active time $\tilde{T}(\Delta t, \mathcal{B}'_p)$, i.e., how long the network was sensitive to domain-walls as a function of pseudo-magnetic field-pulse-magnitude sensitivity, \mathcal{B}'_p , and pulse duration, Δt . A signal with pseudo-magnetic field magnitude \mathcal{B}_p produces a magnitude-to-uncertainty ratio of $\zeta = \mathcal{B}_p/\mathcal{B}'_p$. The characteristic shape of the sensitive region is a result of the filtering and averaging of the raw data as described in Sec. IV. Averaging reduces the sensitivity of the search data to short pulse durations and high-pass filtering suppresses sensitivity for long Δt . The GNOME sensitivity varies in time as the number of active GNOME magnetometers recording data and their background noise change. The active time, $\tilde{T}(\Delta t, \mathcal{B}'_p)$,

can be used to constrain ALP domain-wall parameter space as discussed in Appendix A.

If one assumes a probability distribution for the number of domain-wall encounters, an upper bound on the rate R_C of such encounters can be calculated with a confidence level C . We assume a Poisson probability distribution for the domain-wall crossings. Since the excess number of events in the search data as compared to the background data was not statistically significant, the upper bound on the observable rate is given by the probability of measuring no events during the effective time [40]. Note that since \tilde{T} depends on the parameters of the domain-wall crossing, our constraint on the observed rate depends on the ALP properties. We choose the confidence level to be $C = 90\%$.

III. DISCUSSION

The analysis of the GNOME data did not find any statistically significant excess of events above background during Science Run 2 that could point to the existence of ALP domain walls, as seen in Fig. 2. The expected rate of domain-wall encounters, r , depends on the ALP mass, m_a , the domain-wall energy density in the Milky Way, ρ_{DW} , the typical relative domain-wall speed \bar{v} given by the Standard Halo Model, and the symmetry breaking scale, f_{SB} . The region of parameter space to which GNOME is sensitive is defined by the ALP parameters expected to produce signals above 12.6 magnitude-to-uncertainty ratio with rates $r \geq R_{90\%}$ during Science

Run 2 (see Fig. 3). Based on the null result of our search, the sensitive region is interpreted as excluded ALP parameter space.

The ALP parameters and the phenomenological parameters describing the ALP domain walls in our galaxy, namely the thickness Δx , the surface tension or energy per unit area σ_{DW} , and the average separation \bar{L} can be related through the ALP domain wall model described in Refs. [13, 21]. A full derivation of how observable parameters are related to ALP parameters is given in Appendix A and summarized below.

The domain-wall thickness is determined by the ALP mass, and is on the order of the ALP reduced Compton wavelength λ_a [21],

$$\Delta x \approx 2\sqrt{2}\lambda_a = 2\sqrt{2}\frac{\hbar}{m_a c} . \quad (5)$$

The constant prefactor of $2\sqrt{2}$ is obtained by approximating the spatial profile of the field-gradient magnitude as a Lorentzian and defining the thickness as full width at half maximum. For a given relative velocity component perpendicular to the domain wall v_{\perp} , the signal duration is

$$\Delta t = \frac{\Delta x}{v_{\perp}} \propto m_a^{-1} . \quad (6)$$

We assume that domain walls comprise the dominant component of dark matter. Thus with the energy density $\rho_{\text{DW}} \approx 0.4 \text{ GeV}/\text{cm}^3$ in the Milky Way [23], the energy per unit area (surface tension) in a domain wall, σ_{DW} , determines the average separation between domain walls, \bar{L} . The surface tension σ_{DW} is related to the symmetry breaking scale [13],

$$\sigma_{\text{DW}} = \frac{8}{\hbar^2} m_a f_{\text{SB}}^2 . \quad (7)$$

The average domain-wall separation is then approximated by

$$\bar{L} \approx \frac{\sigma_{\text{DW}}}{\rho_{\text{DW}}} = \frac{8}{\hbar^2} \frac{m_a f_{\text{SB}}^2}{\rho_{\text{DW}}} , \quad (8)$$

which results in the average domain-wall encounter rate,

$$r = \bar{v}/\bar{L} \propto (m_a f_{\text{SB}}^2)^{-1} . \quad (9)$$

The colored region in Fig. 4a describes the symmetry breaking scales up to which GNOME was sensitive with 90% confidence (as detailed in Appendix A). The parameter space is spanned by ALP mass, maximum symmetry breaking scale, and ratio between symmetry breaking scale and coupling constant. The shape of the sensitive area shown in Fig. 4a is determined by the event with the largest magnitude-to-uncertainty and the characteristics of the preprocessing applied to the raw data.

Figure 4b shows various cross-sections of Fig. 4a for different ratios between the symmetry breaking scale and

the coupling constant indicated by the dashed lines. The upper bound of f_{SB} that can be observed by the network is shown in Fig. 4b for different ratios $\xi \equiv f_{\text{SB}}/f_{\text{int}}$. Because $\mathcal{B}_{\text{p}} \propto m_a$ [see Eq. (A.10)], there is a sharp cut-off for low ALP mass where the corresponding field magnitude falls below the network sensitivity. Even though \mathcal{B}_{p} increases for large m_a , the mean rate of domain-wall encounters decreases with increasing mass [see Eqs. (8) and (9)]. Correspondingly, the upper limit for the symmetry-breaking scale f_{SB} is $\propto 1/\sqrt{m_a}$. Given that no events were found, the sensitive region of ALP-domain-wall parameter space during Science Run 2 can be excluded.

Our experiment explores ALP parameter space up to $f_{\text{int}} \sim 3 \times 10^5 \text{ GeV}$ (see Fig. 4). This goes beyond that excluded by previous direct laboratory experiments searching for ALP-mediated exotic pseudoscalar interactions between protons which have shown that $f_{\text{int}} \gtrsim 300 \text{ GeV}$ over the ALP mass range probed by the GNOME [41]. Although astrophysical observations suggest that $f_{\text{int}} \gtrsim 2 \times 10^8 \text{ GeV}$, there are a variety of scenarios in which such astrophysical constraints can be evaded [42, 43].

Future work of the GNOME collaboration will focus both on upgrades to our experimental apparatus and new data-analysis strategies. One of our key goals is to improve overall reliability and the duration of continuous operation of GNOME magnetometers³. Additionally, magnetometers varied in their bandwidths and reliability, and stability of their calibration. These challenges were addressed in Science Run 4 through a variety of magnetometer upgrades and instituting daily worldwide test and calibration pulse sequences. However GNOME suffered disruptions due to the worldwide COVID-19 pandemic. We plan to carry out Science Run 5 in 2021 to take full advantage of the improvements. Furthermore, by upgrading to noble-gas-based comagnetometers [44, 45] for future science runs (Advanced GNOME), we expect to significantly improve the sensitivity to ALP domain walls. Additionally, GNOME data can be searched for other signatures of physics beyond the Standard Model such as boson stars [17], relaxation halos [46], and bursts of exotic low-mass fields from black-hole mergers [30]. In terms of the data-analysis algorithm used to search for ALP domain walls, in future work we aim to improve the efficiency of the scan over the velocity lattice. The number of points in the velocity lattice to reliably cover a fixed fraction (e.g., 97.5%) of the ALP velocity probability distribution grows as $(\Delta t)^{-3}$ [where Δt is given by Eq. (6)]. This makes the algorithm computationally intensive. We are investigating a variety of new analysis approaches, such as machine-learning-based algorithms, to address these issues.

³ The intermittent operation of some magnetometers due to technical difficulties during Science Runs 1-3 made it difficult to search for signals persisting $\gtrsim 1$ hour.

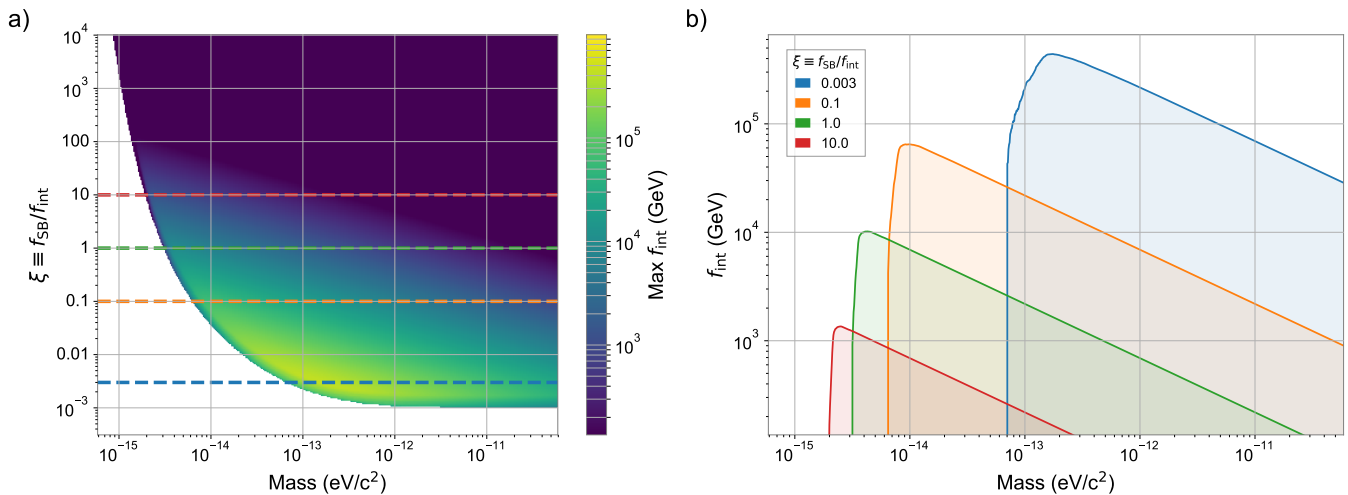


Figure 4. Parameter space of the ALP constrained by the presented analysis of Science Run 2 with 90% confidence level (see Sec. II). The relationship between ALP theory parameters and measured quantities are discussed in Sec. III and Appendix A. (a) In color, upper bound on the the interaction scale, f_{int} , to which the GNOME was sensitive as a function of m_a and the ratio $\xi \equiv f_{\text{SB}}/f_{\text{int}}$. (b) Cross-sections of the excluded parameter volume in (a) for different ratios ξ represented by the corresponding dashed lines of the matching color in (a).

IV. METHODS

462

463 The GNOME consists of over a dozen optical atomic
 464 magnetometers, each enclosed within a multi-layer mag-
 465 netic shield, distributed around the world [26]. GNOME
 466 magnetometers are based on a variety of different atomic
 467 species, optical transitions, and measurement techniques:
 468 some are frequency- or amplitude-modulated nonlinear
 469 magneto-optical rotation magnetometers (NMOR) [47,
 470 48], some are rf-driven optical magnetometers [24], while
 471 others are spin-exchange-relaxation-free magnetometers
 472 (SERF) [49]. A detailed description and characterization
 473 of six GNOME magnetometers is given in Ref. [24]. A
 474 summary of the properties of the GNOME magnetome-
 475 ters active during Science Run 2 is presented in Table I.

476 Each GNOME station is equipped with auxiliary
 477 sensors, including accelerometers, gyroscopes, and un-
 478 shielded magnetometers, to measure local perturbations
 479 that could mimic a dark matter signal. Suspicious data
 480 are flagged [24] and discarded during the analysis.

481 The number of active GNOME magnetometers during
 482 the four Science Runs and the combined network noise as
 483 defined in Ref. [29] is shown as a function of time in Fig. 5.
 484 The data in Science Run 4, although they extended for a
 485 longer period of time, featured poorer noise characteris-
 486 tics and consistency of operation to Science Run 2. Since
 487 many GNOME stations underwent upgrades in 2018 and
 488 2019, further characterization of Science Run 4 data is
 489 needed, and results will be presented in future work.

490 Here we provide more details on the analysis proce-
 491 dure discussed in Sec. II. It is composed of three stages to
 492 identify events likely to be produced by ALP domain-wall
 493 crossings: preprocessing, velocity scanning, and post-
 494 selection [29]. First, in the preprocessing stage, a rolling

495 average and filters are applied to the GNOME magne-
 496 tometer raw data which are originally recorded by the
 497 GPS-synchronized data-acquisition system at a rate of
 498 512 samples/s [25]. The rolling average is characterized
 499 by a 20 s time constant. Noisy frequency bands are sup-
 500 pressed using a first-order Butterworth high-pass filter at
 501 1.67 mHz together with the notch filters corresponding
 502 to 50 Hz and 60 Hz power line frequencies with a quality
 503 factor of 60. These filters are applied forward and back-
 504 ward to remove phase effects. This limits the observable
 505 pulse properties to a frequency region to which all mag-
 506 netometers are sensitive. Additionally, it guarantees that
 507 the duration of the signal is the same in all sensors. We
 508 note that these filter settings may be changed in future
 509 analysis.

510 The local standard deviation around each point in
 511 the magnetometer's data is determined using an iterat-
 512 ive process. Outliers are discarded until the standard
 513 deviation of the data in the segment converges. The
 514 local standard deviation is calculated taking 100 down-
 515 sampled points around each data point.

516 Additionally, auxiliary measurements have shown that
 517 the calibration factors used by each magnetometer to
 518 convert raw data into magnetic field units experience
 519 change over time due to, for example, changes in the en-
 520 vironmental conditions. Upper limits on the calibration
 521 factor errors due to such drifts over the course of Science
 522 Run 2 have been evaluated and are listed in Table I. Cali-
 523 bration factor errors result in magnetic field measurement
 524 errors proportional to the magnetic field B_j . The uncer-
 525 tainty resulting from the calibration error is later used to
 526 determine agreement with the domain-wall model, but
 527 not in the magnitude-to-uncertainty ratio estimate re-
 528 sulting from the model, since the calibration error affects

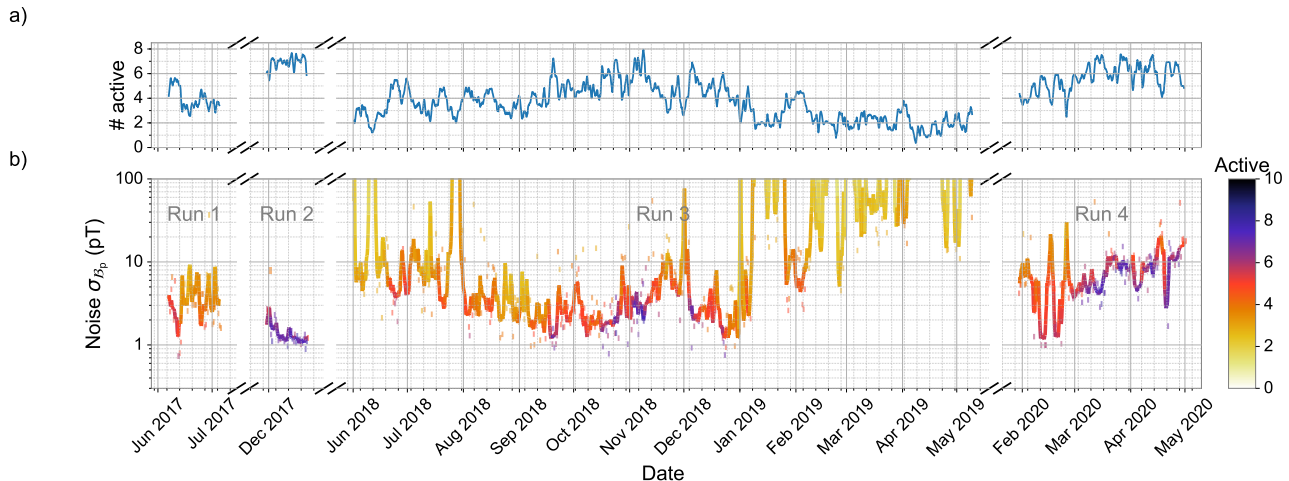


Figure 5. Summary of the GNOME performance during the four Science Runs from 2017 to 2020. The raw magnetometer data are averaged for 20s and their standard deviation is calculated over a minimum of one and a maximum of two hours segments depending on the availability of continuous data segments. For each binned point, the combined network noise considering the worse case domain-wall crossing direction is evaluated as defined in Ref. [29]. (a) One-day rolling average of the number of active sensors. (b) Multi-colored solid line represents the one-day rolling average of the combined network noise and the multi-colored dashes show the noise of the individual sampled segments. The data are preprocessed with the same filters used for the analysis. The number of magnetometers active is indicated by the color of the line and dashes.

Table I. Characteristics of the magnetometers active during Science Run 2 (see, e.g., Fig. 5). The station name, location in longitude and latitude, orientation of the sensitive axis, type of magnetometer (NMOR [47, 48], rf-driven [24], or SERF [49]), and probed transition are listed. The bandwidth indicates the measured -3dB point of the magnetometers' frequency response to oscillating magnetic fields. The calibration error takes into account potential temporal variation of the magnetometers' calibration over the course of Science Run 2, and is estimated based on auxiliary measurements. The rightmost column lists the estimated ratio between the effective proton spin polarization and the Landé g -factor for the magnetometer, σ_p/g , which depends on the atomic species and the magnetometry scheme as described in Appendix B. The σ_p/g value is used to relate the measured magnetic field to the signal expected from the interaction of an ALP field with proton spins. The indicated uncertainty describes the range of values from different theoretical calculations [28].

Station	Location		Orientation		Type	Probed transition	Bandwidth	Cal. Error	σ_p/g
	Longitude	Latitude	Az	Alt					
Beijing	116.1868° E	40.2457° N	+251°	0°	NMOR	^{133}Cs D2 F=4	115 Hz	20%	$-0.39_{-0.00}^{+0.19}$
Berkeley	122.2570° W	37.8723° N	0°	+90°	NMOR	^{133}Cs D2 F=4	7 Hz	40%	$-0.39_{-0.00}^{+0.19}$
Daejeon	127.3987° E	36.3909° N	0°	+90°	NMOR	^{133}Cs D2 F=4	10 Hz	20%	$-0.39_{-0.00}^{+0.19}$
Fribourg	7.1581° E	46.7930° N	+190°	0°	rf-driven	^{133}Cs D1 F=4	94 Hz	5%	$-0.39_{-0.00}^{+0.19}$
Hayward	122.0539° W	37.6564° N	0°	-90°	NMOR	^{85}Rb D2 F=3	37 Hz	5%	$-0.36_{-0.00}^{+0.05}$
Hefei	117.2526° E	31.8429° N	+90°	0°	SERF	^{85}Rb & ^{87}Rb D1	127 Hz	5%	$-0.38_{-0.00}^{+0.05}$
Krakow	19.9048° E	50.0289° N	+45°	0°	NMOR	^{87}Rb D1 F=2	3 Hz	20%	$0.50_{-0.11}^{+0.00}$
Lewisburg	76.8825° W	40.9557° N	0°	+90°	SERF	^{87}Rb D2	200 Hz	10%	$0.70_{-0.15}^{+0.00}$
Mainz	8.2354° E	49.9915° N	0°	-90°	NMOR	^{87}Rb D2 F=2	99 Hz	2%	$0.50_{-0.11}^{+0.00}$

529 signal and noise in the same way.

530 Second, in the velocity-scanning stage, the data from
 531 the individual magnetometers are time-shifted according
 532 to different relative velocities between Earth and the ALP
 533 domain walls. In order to sample 97.5% of the velocity
 534 probability distribution, a scan of the speeds from 53.7

535 to 770 km/s with directions covering the full 4π solid
 536 angle is chosen. Note that this distribution considers just
 537 the observable perpendicular component of the relative
 538 domain-wall velocity and neglects the orbital motion of
 539 the Earth around the Sun. For low relative velocities,
 540 both the time between signals at different magnetometers

541 as well as the signal duration diverge. So the velocity
542 range is determined by the chosen 97.5% coverage and
543 the maximum relative speed of domain walls travelling
544 at the galactic escape speed.

545 The corresponding time-shifted data along with their
546 local standard deviation estimate are fetched from each
547 magnetometer’s rolling averaged full-rate data at a rate
548 of 0.1 samples/s. This reduces the amount of data to
549 process, while keeping the full timing resolution.

550 The step size used in the speed scan is chosen so that
551 a single step in speed corresponds to time-shift differ-
552 ences of less than the down-sampled sampling period.
553 For each speed, a lattice of directions covering the full
554 4π solid angle is constructed. The angular difference be-
555 tween adjacent directions is informed by sampling rate
556 and speed [29] such that, as for the speed scan, a single
557 step in direction results in time-shift differences of less
558 than the down-sampled sampling period. With the set-
559 tings used, the velocity-scanning lattice consists of 1661
560 points. This number scales with the down-sampled sam-
561 pling rate cubed.

562 After time-shifting, the pulses produced by a domain-
563 wall crossing appear simultaneously as if all the magne-
564 tometers were placed at the Earth’s center. This process
565 results in a time-shifted data set for each lattice veloc-
566 ity on which for each time point a χ^2 -minimization is
567 performed to estimate the domain-wall parameters. An
568 ALP domain-wall-crossing direction and magnitude, \mathcal{B}_p ,
569 with the corresponding p -value quantifying the agree-
570 ment is obtained. The p -value is evaluated as the prob-
571 ability of obtaining the given χ^2 value or higher from
572 the χ^2 -minimization. The p -value is calculated using the
573 quadrature sum of the standard deviation of the data and
574 the uncertainty due to drifts of the calibration factors.
575 All data points in every time-shifted data set are consid-
576 ered potential events, characterized by time, p -value as
577 well as direction and magnitude \mathcal{B}_p with their associated
578 uncertainties. The magnitude-to-uncertainty ratio of an
579 event ζ is the ratio between this \mathcal{B}_p and its associated
580 uncertainty.

581 Third, in the post-selection stage, two tests are carried
582 out to check if a potential event is consistent with an
583 ALP domain-wall crossing. The domain-wall model test
584 evaluates if the observed signal amplitudes are consistent
585 with the expected pattern of a domain-wall crossing from
586 any possible direction. It is quantified by the aforemen-
587 tioned p -value. The directional-consistency test is based
588 on the angular difference between the estimated domain-
589 wall crossing direction and the direction of the velocity
590 corresponding to the particular time-shifted data set be-
591 ing analyzed. In a real domain-wall crossing event, these
592 two directions should be aligned.

593 To evaluate the consistency of a potential event with
594 a domain-wall crossing, we impose thresholds on the p -
595 value and the angular difference normalized with respect
596 to the angular spacing of the lattice of velocity points for
597 that speed. The thresholds are chosen to guarantee a de-
598 tection probability of 97.5% with the minimum possible

599 false-positive probability. The false-positive analysis is
600 performed on the background data. The true-positive
601 analysis is performed on test data consisting of back-
602 ground data with randomly inserted domain wall signals
603 as we describe below.

604 A single signal pattern may appear as multiple po-
605 tential events in the analysis, whereas we are seeking
606 to characterize a single underlying domain-wall crossing
607 event. For example, a signal consistent with a domain-
608 wall crossing lasting for multiple sampling periods would
609 appear as multiple potential events in a single time-
610 shifted data set. Furthermore, even if such a signal lasts
611 for only a single sampling period, corresponding potential
612 events appear in different time-shifted data sets. Since
613 it is assumed that domain-wall crossings occur rarely,
614 such clusters of potential events are classified as a sin-
615 gle “event.” In order to reduce double-counting of these
616 events, conditions are imposed. If potential events pass-
617 ing the thresholds occur at the same time in different
618 time-shifted data sets or are contiguous in time, the po-
619 tential event with the greatest magnitude-to-uncertainty
620 ratio is classified as the corresponding single event.

621 The true-positive analysis studies the detection prob-
622 ability as a function of the thresholds. Multiple test
623 data sets are created featuring domain-wall-signal pat-
624 terns with random parameters by inserting Lorentzian-
625 shaped pulses into the background data of the different
626 GNOME magnetometers. The domain-crossing events
627 have magnitudes of \mathcal{B}_p randomly selected between 0.1 pT
628 and 10^4 pT and durations randomly selected between
629 0.01 s and 10^3 s. The distributions of the these ran-
630 domized parameters are chosen to be flat on a logarith-
631 mic scale. Additionally, the signals are inserted at ran-
632 dom times with random directions. In order to simulate
633 calibration error effects, the pulse amplitudes inserted
634 in each magnetometer are weighted by a random factor
635 whose range is given in Table I. The crossing velocity is
636 also randomized within the range covered by the veloc-
637 ity lattice. For each inserted domain-wall-crossing event,
638 the p -value, the normalized angular difference, and the
639 magnitude-to-uncertainty ratio are computed.

640 Figure 6a shows the detection probability as a func-
641 tion of the threshold on the lower-limit of the p -value
642 and the threshold on the upper-limit of the normalized
643 angular difference. We restrict the analysis in Fig. 6a
644 to events inserted with a magnitude-to-uncertainty ra-
645 tio between 5 and 10. This enables reliable determina-
646 tion of the true-positive detection probability without
647 significant contamination by false positive events since
648 the background event probability above $\zeta = 5$ is below
649 0.01% in a 10s sampling interval. Since the detection
650 probability increases with the signal magnitude, we fo-
651 cus on the events below $\zeta = 10$. The detection proba-
652 bility is then the number of detected events divided by
653 the number of inserted events. The black line marks the
654 numerically evaluated boundary of the area guaranteeing
655 at least 97.5% detection. All points along this black line
656 will yield the desired detection probability, so the partic-

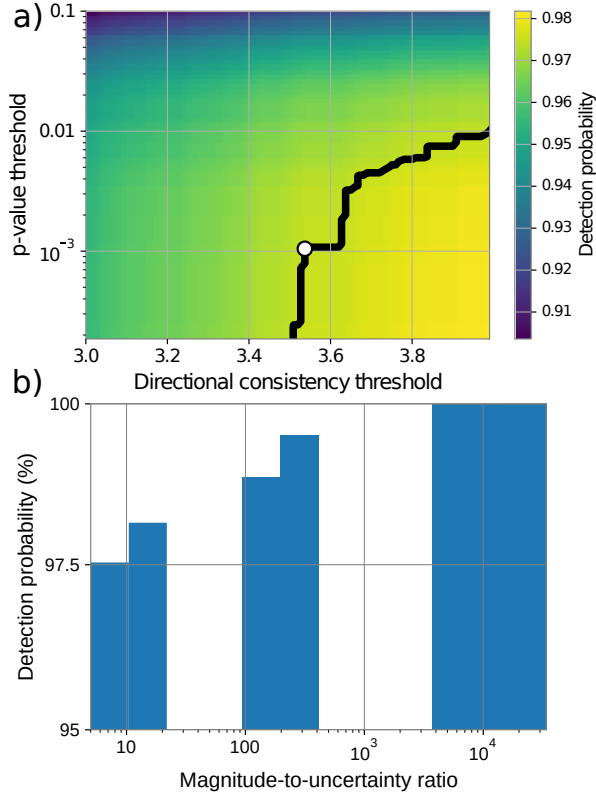


Figure 6. Summary of the true-positive analysis results. (a) shows the probability of detecting a domain-wall-crossing event with randomized parameters (as discussed in the text) as a function of p -value and directional-consistency thresholds. The inserted events have a magnitude-to-uncertainty ratio between 5 and 10. The black line indicates the combination of parameters corresponding to a 97.5% detection probability. The white dot indicates the particular thresholds chosen for the analysis. (b) Shows the mean detection probability reached for different magnitude-to-uncertainty ratios for the chosen thresholds.

ular choice is made to minimize the number of candidate events when applying the search algorithm to background data. These values are 0.001 for the p -value threshold and 3.5 for the directional-consistency threshold (represented as a white dot in Fig. 6a). Figure 6b shows that the detection probability is greater than 97.5% for events featuring a magnitude-to-uncertainty ratio above 5 and guarantees $\epsilon \geq 95\%$.

Since the noise has a nonzero probability of mimicking the signal pattern expected from an ALP domain-wall crossing well enough to pass the p -value and directional consistency tests, we perform a false-positive study on background data. The analysis algorithm is applied to $T_b=10.7$ years of time-shuffled data in order to establish the rate of events expected solely from background. Because of the larger amount of background data analyzed, lower rates and larger magnitude-to-uncertainty ratios are accessible as compared to the search data. Based on the false positive study, the probability of finding one or

more events in the search data above ζ , is [50],

$$P(\geq 1 \text{ above } \zeta) = 1 - \exp\left(-\frac{T}{T_b} [1 + n_b(\zeta)]\right), \quad (10)$$

where $T = 23$ days is the duration of Science Run 2 and $n_b(\zeta)$ is the number of candidate events found in the background data above ζ . The significance is then defined as, $S = -\sqrt{2} \operatorname{erf}^{-1} [1 - 2(1 - P)]$, where erf^{-1} is the inverse error function. The significance is given in units of the Gaussian standard deviation which corresponds to a one-sided probability of P .

After characterizing the background for Science Run 2, the search data are analyzed. The results are represented as a solid green line in Fig. 2. For $\zeta > 6$ only a few events were found. The event with largest magnitude-to-uncertainty ratio, ζ_{\max} was measured at 12.6 followed by additional events at 6.2 and 5.6. From Eq. (10), the significance associated with finding one or more events produced by the background featuring at least ζ_{\max} is lower than one sigma. This null result defines the sensitivity of the search and is used to set constraints on the parameter space describing ALP domain walls.

The observable rate of domain-wall crossings depends on how long GNOME was sensitive to different signal durations and magnitudes. For the evaluation of this effective time, the raw data of each magnetometer are divided into continuous segments between one to two hours duration depending on the availability of the data. The preprocessing steps are applied to each segment. Then the data are binned by taking the average in 20 s intervals. To estimate the noise in each magnetometer, the standard deviation in each binned segment is calculated to define the covariance matrix Σ_s . The domain-wall magnitude, crossing with the worse case direction \hat{m} , needed to produce $\zeta = 1$ is calculated as in Ref. [29],

$$\mathcal{B}'_p(\Delta t) = \sqrt{\hat{m} (D_{\Delta t}^T \Sigma_s^{-1} D_{\Delta t})^{-1} \hat{m}}, \quad (11)$$

for each bin. The matrix $D_{\Delta t}$ contains the sensitivity axes of the magnetometers, the factor σ_p/g , and the effects of the preprocessing as a function of the signal duration as described in Ref. [29]. Such preprocessing effects rely on a Lorentzian-shaped signal and give rise to the characteristic shape of Fig. 3. The effective time, \tilde{T} , is defined as the amount of time the network can measure a domain wall with duration Δt and magnitude \mathcal{B}'_p producing $\zeta \geq 1$. Monte Carlo simulations analyzing segments with inserted domain-wall encounters on raw data show a good agreement with the sensitivity estimation in Eq. (11).

Assuming that the domain-wall encounters follow Poisson statistics, a bound on the observable rate of events above ζ_{\max} with 90% confidence is set as [40],

$$R_{90\%} = \frac{-\log(0.1)}{\epsilon \tilde{T}(\Delta t, \mathcal{B}'_p)}. \quad (12)$$

The ALP parameter space is constrained by imposing that $r \geq R_{90\%}$. The experimental constraint on the

725 coupling constant is written as (see Eq. (A.13) in Ap-
726 pendix A),

$$f_{\text{int}} \leq \frac{\hbar}{\xi} \sqrt{\frac{\bar{v}\rho_{\text{DW}}\epsilon}{8m_a \log(0.1)}} \tilde{T}(\Delta t, \mathcal{B}'_p) \quad (13)$$

727 The signal duration can be written in terms of the mass
728 of the hypothetical ALP particle and the specific domain-
729 wall crossing speed, $\Delta t = \frac{2\sqrt{2}\hbar}{\bar{v}m_a c}$. When calculating the
730 constraints on f_{int} , we fix the domain-wall crossing speed
731 to the typical relative speed from the Standard Halo
732 Model, $\bar{v} = 300 \text{ km s}^{-1}$ [31]. In contrast to the sig-
733 nal duration, the pseudo-magnetic field signal depends
734 on all parameters of the ALPs, the mass and the ra-
735 tio between the coupling and symmetry breaking con-
736 stants, $\mathcal{B}'_p = \frac{4m_a c^2 \xi}{\mu_B \zeta}$. Figure 4 is given by Eq. (13) taking
737 $\zeta = 12.6$. The shape of the constrained space is given by
738 the fact that \tilde{T} varies depending on the target m_a and ξ .
739 A detailed derivation of Eq. (13) is given in Appendix A.

740 ACKNOWLEDGMENTS

741 The authors are grateful to Chris Pankow, Joshua
742 R. Smith, Jocelyn Read, Menachem Givon, Ron Fol-

743 man, Wojciech Gawlik, Kathryn Grimm, Grzegorz
744 Łukasiewicz, Peter Fierlinger, Volkmar Schultze, Tilman
745 Sander-Thömes, and Holger Müller for insightful discus-
746 sions.

747 This work was supported by the U.S. National Sci-
748 ence Foundation under grants PHY-1707875 and PHY-
749 1707803, the Swiss National Science Foundation under
750 grant No. 200021 172686, the German research founda-
751 tion under grant no. 439720477, the European Research
752 Council under the European Union's Horizon 2020 Re-
753 search and Innovative Program under Grant agreement
754 No. 695405, the Cluster of Excellence PRISMA+, DFG
755 Reinhart Koselleck Project, Simons Foundation, a Fun-
756 damental Physics Innovation Award from the Gordon
757 and Betty Moore Foundation, Heising-Simons Founda-
758 tion, the National Science Centre of Poland within the
759 OPUS program (Project No. 2015/19/B/ST2/02129),
760 and IBS-R017-D1-2021-a00 of the Republic of Korea.

-
- 761 [1] G. Bertone, D. Hooper, and J. Silk, Particle dark matter:
762 Evidence, candidates and constraints, *Phys. Rep.* **405**,
763 279 (2005).
764 [2] J. L. Feng, Dark matter candidates from particle physics
765 and methods of detection, *Annu. Rev. Astron. Astrophys.*
766 **48**, 495 (2010).
767 [3] P. Gorenstein and W. Tucker, Astronomical signatures
768 of dark matter, *Adv. High Energy Phys.* **2014**, 878203
769 (2014).
770 [4] M. Safronova, D. Budker, D. DeMille, D. F. Jackson Kim-
771 ball, A. Derevianko, and C. W. Clark, Search for new
772 physics with atoms and molecules, *Rev. Mod. Phys.* **90**,
773 025008 (2018).
774 [5] J. Preskill, M. B. Wise, and F. Wilczek, Cosmology of
775 the invisible axion, *Phys. Lett. B* **120**, 127 (1983).
776 [6] L. F. Abbott and P. Sikivie, A cosmological bound on
777 the invisible axion, *Phys. Lett. B* **120**, 133 (1983).
778 [7] M. Dine and W. Fischler, The not-so-harmless axion,
779 *Phys. Lett. B* **120**, 137 (1983).
780 [8] P. W. Graham, I. G. Irastorza, S. K. Lamoreaux, A. Lind-
781 ner, and K. A. van Bibber, Experimental searches for the
782 axion and axion-like particles, *Annu. Rev. Nucl. Part.*
783 *Sci.* **65**, 485 (2015).
784 [9] P. W. Graham, D. E. Kaplan, and S. Rajendran, Cos-
785 mological relaxation of the electroweak scale, *Phys. Rev.*
786 *Lett.* **115**, 221801 (2015).
787 [10] R. T. Co, L. J. Hall, and K. Harigaya, Predictions
788 for axion couplings from alp cogenesis, arXiv:2006.04809
789 (2020).
790 [11] P. Sikivie, Axions, domain walls, and the early universe,
791 *Phys. Rev. Lett.* **48**, 1156 (1982).
792 [12] A. Vilenkin, Cosmic strings and domain walls, *Phys. Rep.*
793 **121**, 263 (1985).
794 [13] M. Pospelov, S. Pustelny, M. P. Ledbetter, D. F. Jack-
795 son Kimball, W. Gawlik, and D. Budker, Detecting do-
796 main walls of axionlike models using terrestrial experi-
797 ments, *Phys. Rev. Lett.* **110**, 021803 (2013).
798 [14] M. Kawasaki, K. Saikawa, and T. Sekiguchi, Axion dark
799 matter from topological defects, *Phys. Rev. D* **91**, 065014
800 (2015).
801 [15] D. J. Kaup, Klein-gordon geon, *Phys. Rev.* **172**, 1331
802 (1968).
803 [16] E. Braaten, A. Mohapatra, and H. Zhang, Dense axion
804 stars, *Phys. Rev. Lett.* **117**, 121801 (2016).
805 [17] D. Jackson Kimball, D. Budker, J. Eby, M. Pospelov,
806 S. Pustelny, T. Scholtes, Y. Stadnik, A. Weis, and
807 A. Wickenbrock, Searching for axion stars and q-balls
808 with a terrestrial magnetometer network, *Phys. Rev. D*
809 **97**, 043002 (2018).
810 [18] A. Derevianko and M. Pospelov, Hunting for topologi-
811 cal dark matter with atomic clocks, *Nat. Phys.* **10**, 933
812 (2014).
813 [19] S. Coleman, Q-balls, *Nucl. Phys. B* **262**, 263 (1985).
814 [20] A. Kusenko and P. J. Steinhardt, Q-ball candidates for
815 self-interacting dark matter, *Phys. Rev. Lett.* **87**, 141301
816 (2001).
817 [21] S. Pustelny, D. F. Jackson Kimball, C. Pankow, M. P.
818 Ledbetter, P. Włodarczyk, P. Wcisło, M. Pospelov, J. R.
819 Smith, J. Read, W. Gawlik, and D. Budker, The global
820 network of optical magnetometers for exotic physics
821 (gnome): A novel scheme to search for physics beyond
822 the standard model, *Ann. Phys. (Berl.)* **525**, 659 (2013).
823 [22] B. M. Roberts, G. Blewitt, C. Dailey, M. Murphy,
824 M. Pospelov, A. Rollings, J. Sherman, W. Williams, and

- 825 A. Derevianko, Gps as a dark matter detector: Orders- 889
 826 of-magnitude improvement on couplings of clumpy dark 890
 827 matter to atomic clocks, arXiv:1704.06844, Nat. Com- 891
 828 mun. (2017). 892
- 829 [23] J. Bovy and S. Tremaine, On the local dark matter den- 893
 830 sity, *Astrophys. J.* **756**, 89 (2012). 894
- 831 [24] S. Afach, D. Budker, G. DeCamp, V. Dumont, Z. D. 895
 832 Grujić, H. Guo, D. Jackson Kimball, T. Kornack, 896
 833 V. Lebedev, W. Li, *et al.*, Characterization of the global 897
 834 network of optical magnetometers to search for exotic 898
 835 physics (gnome), *Phys. Dark Universe* **22**, 162 (2018). 899
- 836 [25] P. Włodarczyk, S. Pustelny, D. Budker, and M. Lipiński, 900
 837 Multi-channel data acquisition system with absolute time 901
 838 synchronization, *Nucl. Instr. Meth. Phys. Res. A* **763**, 902
 839 150 (2014). 903
- 840 [26] V. V. Yashchuk, S.-K. Lee, and E. Paperno, Magnetic 904
 841 shielding, in *Optical Magnetometry*, edited by D. Budker 905
 842 and D. F. Jackson Kimball (Cambridge University Press, 906
 843 2013) Chap. 12. 907
- 844 [27] D. F. Jackson Kimball, J. Dudley, Y. Li, S. Thulasi, 908
 845 S. Pustelny, D. Budker, and M. Zolotorev, Magnetic 909
 846 shielding and exotic spin-dependent interactions, *Phys.* 910
 847 *Rev. D* **94**, 082005 (2016). 911
- 848 [28] D. F. Jackson Kimball, Nuclear spin content and con- 912
 849 straints on exotic spin-dependent couplings, *New J. Phys.* 913
 850 **17**, 073008 (2015). 914
- 851 [29] H. Masia-Roig, J. A. Smiga, D. Budker, V. Dumont, 915
 852 Z. Grujić, D. Kim, D. F. Jackson Kimball, V. Lebedev, 916
 853 M. Monroy, S. Pustelny, T. Scholtes, P. C. Segura, Y. K. 917
 854 Semertzidis, Y. C. Shin, J. E. Stalnaker, I. Sulai, A. Weis, 918
 855 and A. Wickenbrock, Analysis method for detecting topo- 919
 856 logical defect dark matter with a global magnetometer 920
 857 network, *Phys. Dark Universe* **28**, 100494 (2020). 921
- 858 [30] C. Dailey, C. Bradley, D. F. Jackson Kimball, I. Sulai, 922
 859 S. Pustelny, A. Wickenbrock, and A. Derevianko, Quan- 923
 860 tum sensor networks as exotic field telescopes for multi- 924
 861 messenger astronomy, *Nat. Astron.* (2020). 925
- 862 [31] B. M. Roberts, G. Blewitt, C. Dailey, M. Murphy, 926
 863 M. Pospelov, A. Rollings, J. Sherman, W. Williams, and 927
 864 A. Derevianko, Search for domain wall dark matter with 928
 865 atomic clocks on board global positioning system satel- 929
 866 lites, *Nat. Commun.* **8**, 1 (2017). 930
- 867 [32] P. Wcisło, P. Morzyński, M. Bober, A. Cygan, D. Lisak, 931
 868 R. Ciuryło, and M. Zawada, Experimental constraint on 932
 869 dark matter detection with optical atomic clocks, *Nat.* 933
 870 *Astron.* **1**, 1 (2016). 934
- 871 [33] B. Roberts, P. Delva, A. Al-Masoudi, A. Amy-Klein, 935
 872 C. Baerentsen, C. Baynham, E. Benkler, S. Bilicki, 936
 873 W. Bowden, E. Cantin, *et al.*, Search for transient vari- 937
 874 ations of the fine structure constant and dark matter 938
 875 using fiber-linked optical atomic clocks, arXiv preprint 939
 876 arXiv:1907.02661 (2019). 940
- 877 [34] Y. V. Stadnik and V. V. Flambaum, Searching for dark 941
 878 matter and variation of fundamental constants with laser 942
 879 and maser interferometry, *Phys. Rev. Lett.* **114**, 161301 943
 880 (2015). 944
- 881 [35] Y. V. Stadnik and V. V. Flambaum, Enhanced effects of 945
 882 variation of the fundamental constants in laser interfer- 946
 883 ometers and application to dark-matter detection, *Phys.* 947
 884 *Rev. A* **93**, 063630 (2016). 948
- 885 [36] D. M. Jacobs, A. Weltman, and G. D. Starkman, Reso- 949
 886 nant bar detector constraints on macro dark matter, 950
 887 *Phys. Rev. D* **91**, 115023 (2015). 951
- 888 [37] A. Arvanitaki, S. Dimopoulos, and K. Van Tilburg, 952
 Sound of dark matter: Searching for light scalars with 953
 resonant-mass detectors, *Phys. Rev. Lett.* **116**, 031102 954
 (2016). 955
- [38] R. L. McNally and T. Zelevinsky, Constraining domain 956
 wall dark matter with a network of superconducting 957
 gravimeters and ligo, *Eur. Phys. J. D* **74**, 1 (2020). 958
- [39] B. P. Abbott, R. Abbott, T. D. Abbott, M. R. Aber- 959
 nathy, F. Acernese, K. Ackley, C. Adams, T. Adams, 960
 P. Addesso, R. X. Adhikari, V. B. Adya, C. Affeldt, 961
 M. Agathos, K. Agatsuma, N. Aggarwal, O. D. Aguiar, 962
 L. Aiello, A. Ain, P. Ajith, B. Allen, A. Allocca, P. A. 963
 Altin, S. B. Anderson, W. G. Anderson, K. Arai, and 964
 Araya (LIGO Scientific Collaboration and Virgo Collab- 965
 oration), Gw150914: First results from the search for 966
 binary black hole coalescence with advanced ligo, *Phys.* 967
Rev. D **93**, 122003 (2016). 968
- [40] P. R. Brady, J. D. E. Creighton, and A. G. Wiseman, Up- 969
 per limits on gravitational-wave signals based on loudest 970
 events, *Class. Quantum Grav.* **21**, S1775 (2004). 971
- [41] N. F. Ramsey, The tensor force between two protons at 972
 long range, *Physica A: Statistical Mechanics and its Ap-* 973
plications **96**, 285 (1979). 974
- [42] W. DeRocco, P. W. Graham, and S. Rajendran, Explor- 975
 ing the robustness of stellar cooling constraints on light 976
 particles, *Phys. Rev. D* **102**, 075015 (2020). 977
- [43] N. Bar, K. Blum, and G. D’amico, Is there a supernova 978
 bound on axions?, *Phys. Rev. D* **101**, 123025 (2020). 979
- [44] T. W. Kornack and M. V. Romalis, Dynamics of two 980
 overlapping spin ensembles interacting by spin exchange, 981
Phys. Rev. Lett. **89**, 253002 (2002). 982
- [45] T. W. Kornack, R. K. Ghosh, and M. V. Romalis, Nu- 983
 clear spin gyroscope based on an atomic comagnetome- 984
 ter, *Phys. Rev. Lett.* **95**, 230801 (2005). 985
- [46] A. Banerjee, D. Budker, J. Eby, H. Kim, and G. Perez, 986
 Relaxion stars and their detection via atomic physics, 987
Commun. Phys. **2** (2020). 988
- [47] D. Budker, D. Kimball, V. Yashchuk, and M. Zolotorev, 989
 Nonlinear magneto-optical rotation with frequency- 990
 modulated light, *Phys. Rev. A* **65**, 055403 (2002). 991
- [48] W. Gawlik, L. Krzemień, S. Pustelny, D. Sangla, J. Za- 992
 chorowski, M. Graf, A. Sushkov, and D. Budker, Nonlin- 993
 ear magneto-optical rotation with amplitude modulated 994
 light, *Appl. Phys. Lett.* **88**, 131108 (2006). 995
- [49] J. Allred, R. Lyman, T. Kornack, and M. V. Roma- 996
 lis, High-sensitivity atomic magnetometer unaffected by 997
 spin-exchange relaxation, *Phys. Rev. Lett.* **89**, 130801 998
 (2002). 999
- [50] S. A. Usman, A. H. Nitz, I. W. Harry, C. M. Biwer, 1000
 D. A. Brown, M. Cabero, C. D. Capano, T. D. Canton, 1001
 T. Dent, S. Fairhurst, M. S. Kehl, D. Keppel, B. Kr- 1002
 ishnan, A. Lenon, A. Lundgren, A. B. Nielsen, L. P. 1003
 Pekowsky, H. P. Pfeiffer, P. R. Saulson, M. West, and 1004
 J. L. Willis, The PyCBC search for gravitational waves 1005
 from compact binary coalescence, *Class. Quantum Grav.* 1006
33, 215004 (2016). 1007
- [51] R. D. Peccei and H. R. Quinn, Cp conservation in the 1008
 presence of instantons, *Phys. Rev. Lett.* **38**, 1440 (1977). 1009
- [52] I. Kominis, T. Kornack, J. Allred, and M. V. Romalis, 1010
 A subfemtotesla multichannel atomic magnetometer, *Nat-* 1011
ure **422**, 596 (2003). 1012
- [53] M. Ledbetter, I. Savukov, V. Acosta, D. Budker, and 1013
 M. Romalis, Spin-exchange-relaxation-free magnetome- 1014
 try with cs vapor, *Phys. Rev. A* **77**, 033408 (2008). 1015

- [54] T. Schmidt, Über die magnetischen momente der atomkerne, *Z. Phys.* **106**, 358 (1937).
- [55] J. Engel and P. Vogel, Spin-dependent cross sections of weakly interacting massive particles on nuclei, *Phys. Rev. D* **40**, 3132 (1989).
- [56] V. Flambaum and A. Tedesco, Dependence of nuclear magnetic moments on quark masses and limits on temporal variation of fundamental constants from atomic clock experiments, *Phys. Rev. C* **73**, 055501 (2006).
- [57] J. Engel, M. Ressel, I. Towner, and W. Ormand, Response of mica to weakly interacting massive particles, *Phys. Rev. C* **52**, 2216 (1995).
- [58] P. Toivanen, M. Kortelainen, J. Suhonen, and J. Toivanen, Large-scale shell-model calculations of elastic and inelastic scattering rates of lightest supersymmetric particles (lsp) on i 127, xe 129, xe 131, and cs 133 nuclei, *Phys. Rev. C* **79**, 044302 (2009).
- [59] F. Iachello, L. M. Krauss, and G. Maino, Spin-dependent scattering of weakly interacting massive particles in heavy nuclei, *Physics Letters B* **254**, 220 (1991).
- [60] L. W. Anderson, F. M. Pipkin, and J. C. Baird Jr, N-14 - N-15 Hyperfine Anomaly, *Phys. Rev.* **116**, 87 (1959).
- [61] W. Happer and H. Tang, Spin-exchange shift and narrowing of magnetic resonance lines in optically pumped alkali vapors, *Phys. Rev. Lett.* **31**, 273 (1973).
- [62] I. Savukov and M. Romalis, Effects of spin-exchange collisions in a high-density alkali-metal vapor in low magnetic fields, *Phys. Rev. A* **71**, 023405 (2005).
- [63] D. Budker, D. F. Kimball, and D. P. DeMille, *Atomic physics: an exploration through problems and solutions* (Oxford University Press, USA, 2008).
- [64] S. Appelt, A. B.-A. Baranga, C. Erickson, M. Romalis, A. Young, and W. Happer, Theory of spin-exchange optical pumping of 3 he and 129 xe , *Phys. Rev. A* **58**, 1412 (1998).

Appendix A: Relating measured parameters to ALP domain-wall parameter space

Domain walls form when a field can monotonically vary across vacuum states; two degenerate vacua or possibly the same state if, for example, the field takes values on the 1-sphere. This is the case for ALPs which arise from the angular part of a complex scalar field [51].

The following Lagrangian terms are considered in natural units ($\hbar = c = 1$ here and throughout this appendix) for a new complex scalar field ϕ ,⁴

$$\mathcal{L} \supset |\partial_\mu \phi|^2 - \frac{\lambda}{S_0^{2N-4}} |2^{N/2} \phi^N + S_0^N|^2, \quad (\text{A.1})$$

where λ is a unitless constant and S_0 is a constant with units of energy [13].

⁴ Other references may use a minus sign in front of the S_0^N term, which results in a similar potential, up to a phase. The end result of Eq. (A.1) is that the axion potential will have a maximum at zero, while the minus-convention will have a vacuum at zero.

The axion field is obtained by reparameterizing the complex field ϕ in Eq. (A.1) in terms of the real field S (Higgs) and a (axion),

$$\phi = \frac{S}{\sqrt{2}} \exp(ia/S_0).$$

The second term in Eq. (A.1) will break the $U(1)$ symmetry of the complex field into a discrete \mathbb{Z}_N symmetry, $\phi \rightarrow \exp(2\pi ik/N)\phi$ for integer k . This corresponds to the axion shift-symmetry, $a \rightarrow a + \frac{2\pi S_0}{N}k$. The Higgs mode obtains a vacuum expectation value $S \rightarrow S_0$, and the axion field has degenerate vacua or ground energy states at $a = \frac{\pi S_0}{N}(2k+1)$ for integer k . One can define the symmetry-breaking scale as $f_{\text{SB}} = S_0/N$. Reparameterizing the complex scalar field in Eq. (A.1) and setting the Higgs mode to the vacuum expectation value, the axion Lagrangian is

$$\mathcal{L}_a = \frac{1}{2}(\partial_\mu a)^2 - 2m_a^2 f_{\text{SB}}^2 \cos^2\left(\frac{a}{2f_{\text{SB}}}\right), \quad (\text{A.2})$$

where the axion mass is $m_a = NS_0\sqrt{2\lambda}$. This can be seen by matching the second-derivative of the cosine term at the minima to a scalar mass term.

For simplicity, a static domain wall in the yz -plane separating domains of $-\pi f_{\text{SB}}$ and $+\pi f_{\text{SB}}$ is considered. Solving the classical field equations, one finds

$$a(x) = 2f_{\text{SB}} \arcsin[\tanh(m_a x)]. \quad (\text{A.3})$$

The gradient of the field is then

$$\frac{da}{dx}(x) = \frac{2f_{\text{SB}}m_a}{\cosh(m_a x)}. \quad (\text{A.4})$$

This has the full width at half maximum,

$$\Delta x = \frac{2 \cosh^{-1}(2)}{m_a} \approx \frac{2\sqrt{2}}{m_a}. \quad (\text{A.5})$$

Using the domain-wall solution [Eq. (A.3)] and integrating the energy density of the domain wall over x yields the surface tension (energy per unit area) [13],

$$\sigma_{\text{DW}} = 8m_a f_{\text{SB}}^2. \quad (\text{A.6})$$

Interactions observable by magnetometers involve coupling between the axion field gradient and the axial-vector current of a fermionic field. For a fermion field ψ , the interaction is

$$\mathcal{L}_{\text{int}} = \frac{i(\phi \partial_\mu \phi^* - \partial_\mu \phi \phi^*)}{S_0 f_{\text{int}}} \bar{\psi} \gamma^\mu \gamma^5 \psi$$

$$\xrightarrow{S \rightarrow S_0} \frac{\partial_\mu a}{f_{\text{int}}} \bar{\psi} \gamma^\mu \gamma^5 \psi. \quad (\text{A.7})$$

The axial-vector current is related to the spin \mathbf{S} , so that the interaction Hamiltonian becomes

$$H_{\text{int}} = \frac{1}{f_{\text{int}}} \nabla a \cdot \frac{\mathbf{S}}{\|\mathbf{S}\|}, \quad (\text{A.8})$$

1033 i.e., for spin- $1/2$ particles, $1/\|S\| = 2$.

1034 Optical magnetometers operate by measuring the
1035 change in atomic energy levels between two energy states
1036 with magnetic quantum numbers differing by Δm_F . A
1037 leading magnetic field is applied to the atoms, and variations
1038 in the magnetic field along the leading field are
1039 measured. The spin coupling from Eq. (A.8) can induce
1040 a similar shift in energy levels to a magnetic field.
1041 The maximum energy shift is determined by plugging the
1042 largest gradient from Eq. (A.4) into Eq. (A.8),

$$\Delta E = \sum_{i \in e, p, n, \dots} \frac{2\eta\sigma_{(i)}\Delta m_F f_{\text{SB}}}{\|S_{(i)}\| f_{\text{int}}^{(i)}} m_a, \quad (\text{A.9})$$

1043 where i labels the species of fermion, $\sigma_{(i)} = \frac{\langle S_{(i)} \cdot F_{(i)} \rangle}{F_{(i)}^2}$
1044 is the projected spin coupling, $\eta = \cos\theta$ for the angle
1045 between the axion gradient and sensitive axis θ , and
1046 $f_{\text{int}}^{(i)}$ is the interaction coupling to particle i . In general,
1047 we will combine the $\frac{\sigma_{(i)}}{\|S_{(i)}\| f_{\text{int}}^{(i)}}$ terms into an effective ratio
1048 $\frac{2\sigma_j}{f_{\text{int}}}$, where j now labels the magnetometer. Comparing
1049 this to the energy shift due to a magnetic field,
1050 $\Delta E_B = g_{F,j}\mu_B\Delta m_F B_j$, one obtains a relationship for a
1051 normalized pseudo-magnetic field,

$$\frac{g_{F,j}B_j}{\sigma_j\eta_j} = \frac{4}{\mu_B} m_a \xi \equiv \mathcal{B}_p, \quad (\text{A.10})$$

1052 for $\xi \equiv \frac{f_{\text{SB}}}{f_{\text{int}}}$, $g_{F,j}$ being the g -factor for the magnetometer
1053 j , and $\|S_{(i)}\| = 1/2$ since we only consider coupling to
1054 spin- $1/2$ particles. Here, the normalization is such that \mathcal{B}_p
1055 is the same for all magnetometers, though each individual
1056 sensor may observe a different pseudo-magnetic field, B_j .

1057 There are two factors that must be considered when
1058 determining if axion domain walls are observable by the
1059 network: the magnitude of the signal \mathcal{B}_p and the rate of
1060 signals. Domain walls are assumed to exist in a static
1061 (or virialized) network across the galaxy through which
1062 Earth traverses. For a domain-wall velocity v , the duration
1063 of a signal is $\Delta t = \Delta x/v$. Filters and bandwidth
1064 limitations generally reduce the magnitude by a factor
1065 dependent on the signal duration, which affects the sensitivity
1066 of the network (see Appendix in Ref. [29]).

1067 Meanwhile, if the domain walls induce a strong enough
1068 signal to be observed, but are so infrequent that one is
1069 unlikely to be found over the course of a measurement,
1070 then the network is effectively insensitive. If the energy
1071 density of domain walls across the galaxy is ρ_{DW} , then
1072 the average rate of domain walls passing through Earth
1073 is given by

$$r = \frac{\bar{v}\rho_{\text{DW}}}{\sigma_{\text{DW}}} = \frac{\bar{v}\rho_{\text{DW}}}{8m_a f_{\text{SB}}^2}, \quad (\text{A.11})$$

1074 where \bar{v} is the typical relative speed.

1075 The physical parameters describing the ALP domain
1076 walls (m_a , f_{SB} , and f_{int}) must be related to the parameters
1077 observable by the network (\mathcal{B}_p and Δt). The energy

1078 density ρ_{DW} and the typical relative speed \bar{v} are assumed
1079 according to the observed dark matter density and
1080 the galactic rotation velocity, respectively.

1081 In order to determine if a set of physical parameters is
1082 observable, the likelihood that no events are found must
1083 be constrained. This constraint defines the confidence
1084 level of the detection. The probability of observing k
1085 events given that one expects to observe μ events is given
1086 by the Poisson probability mass function,

$$P(k; \mu) = \frac{\mu^k}{k!} e^{-\mu}.$$

1087 However, the network also has some detection efficiency
1088 $\epsilon < 1$, so there could be multiple domain-wall-crossing
1089 events, but no detection. In particular, the chance of
1090 missing no events given that there were k events is $(1 - \epsilon)^k$.
1091 For an event rate r and measurement time T , the probability
1092 that no events are detected is then

$$\sum_{k=0}^{\infty} (1 - \epsilon)^k \frac{(rT)^k}{k!} e^{-rT} = e^{-\epsilon rT}.$$

1093 A bound on the event rate R_C at confidence level C is
1094 then given by demanding the probability of observing at
1095 least one event $1 - e^{-\epsilon R_C T} \geq C$, likewise, one would
1096 expect to observe event rates

$$r \geq R_C \equiv \frac{-\log(1 - C)}{\epsilon T}. \quad (\text{A.12})$$

1097 The physical parameter space of the ALPs is constrained
1098 by demanding that $r \geq R_C$. Similar arguments
1099 for defining constraints can be found, e.g., Ref. [40]. The
1100 total time that the network is sensitive to the measurable
1101 parameters, $\tilde{T}(\Delta t, \mathcal{B}'_p)$, may be less than the total
1102 measurement time. These parameters are related to the
1103 physical parameters via Eq. (A.5) and Eq. (A.10). One
1104 finds a sensitivity bound for f_{int} in terms of m_a and ξ ,

$$f_{\text{int}} \leq \frac{1}{\xi} \sqrt{\frac{-\bar{v}\rho_{\text{DW}}\epsilon}{8m_a \log(1 - C)} \tilde{T}(\Delta t, \mathcal{B}'_p)} \quad (\text{A.13})$$

$$\text{for } \Delta t = \frac{2\sqrt{2}}{\bar{v}m_a} \quad \text{and} \quad \mathcal{B}'_p = \frac{4m_a\xi}{\mu_B\zeta},$$

1108 where \mathcal{B}'_p is the sensitivity of the network and ζ is the
1109 magnitude-to-noise ratio induced by a signal with magnitude
1110 \mathcal{B}_p . The main calculation from the network data
1111 needed for this sensitivity bound is \tilde{T} . This is calculated
1112 by measuring the sensitivity of the network over time
1113 for different signal durations Δt and integrating over the
1114 time during which the network is sensitive to $\mathcal{B}_p = \zeta\mathcal{B}'_p$.
1115 Finally, if, after analyzing the data, no domain walls are
1116 found, Eq. (A.13) defines an exclusion region.

Appendix B: Conversion between magnetic field units and proton spin coupling

1117 The amplitude of a signal appearing in the magnetic
1118 field data from a GNOME magnetometer due to interaction
1119 of atomic spins with an ALP field a via the linear

coupling described by Eq. (1) varies based on the atomic species. In every GNOME magnetometer, the vapor cell is located within a multi-layer magnetic shield made of mu-metal and, in some cases a ferrite innermost layer. Interactions of the ALP field with electron spins in the magnetic shielding material can generate a compensating magnetic field that could partially cancel the energy shift due to the interaction of the ALP field with atomic electrons in the vapor cell, as discussed in Ref. [27]. For this reason, GNOME magnetometers are most sensitive to interactions of the ALP field with nuclear spins.

1. Deriving spin-projection

All GNOME magnetometers active during Science Run 2 measure spin-dependent interactions of alkali atoms whose nuclei have valence protons. Thus the GNOME is primarily sensitive to spin-dependent interactions of ALP fields with proton spins. Consequently, the expected signal amplitude measured by a GNOME magnetometer due to the pseudo-magnetic field pulse from passage of Earth through an ALP domain wall must be rescaled by the ratio of the proton spin content of the probed ground-state hyperfine level(s) to their gyromagnetic ratio. Some GNOME magnetometers optically pump and probe a single ground-state hyperfine level, while others rely on the technique of spin-exchange relaxation free (SERF) magnetometry in which the spin-exchange collision rate is much faster than the Larmor precession frequency [49, 52, 53]. For SERF magnetometers a weighted average of the ground-state Zeeman sub-levels over both ground-state hyperfine levels is optically pumped and probed.

Table II shows the relevant factors needed to convert the magnetic field signal recorded by GNOME magnetometers into the expected pseudo-magnetic field due to interaction of an ALP field with the proton spin. Detailed calculations are carried out in Ref. [28]. The relationship of the expectation value for total atomic angular momentum $\langle \mathbf{F} \rangle$ to the nuclear spin $\langle \mathbf{I} \rangle$ can be estimated based on the Russell-Saunders LS -coupling scheme:

$$\begin{aligned} \langle \mathbf{F} \rangle &= \langle \mathbf{S}_e \rangle + \langle \mathbf{L} \rangle + \langle \mathbf{I} \rangle, \\ &= \frac{\langle \mathbf{S}_e \cdot \mathbf{F} \rangle}{F(F+1)} \langle \mathbf{F} \rangle + \frac{\langle \mathbf{L} \cdot \mathbf{F} \rangle}{F(F+1)} \langle \mathbf{F} \rangle + \frac{\langle \mathbf{I} \cdot \mathbf{F} \rangle}{F(F+1)} \langle \mathbf{F} \rangle, \end{aligned} \quad (\text{B.1})$$

where \mathbf{S}_e is the electronic spin and \mathbf{L} is the orbital angular momentum. GNOME magnetometers pump and probe atomic states with $L = 0$, which simplifies the above equation to:

$$\langle \mathbf{F} \rangle = \frac{\langle \mathbf{S}_e \cdot \mathbf{F} \rangle}{F(F+1)} \langle \mathbf{F} \rangle + \frac{\langle \mathbf{I} \cdot \mathbf{F} \rangle}{F(F+1)} \langle \mathbf{F} \rangle. \quad (\text{B.2})$$

For $L = 0$ the projection of \mathbf{I} on \mathbf{F} is given by

$$\langle \mathbf{I} \cdot \mathbf{F} \rangle = \frac{1}{2} [F(F+1) + I(I+1) - S_e(S_e+1)]. \quad (\text{B.3})$$

The above relations define the fractional spin polarization of the nucleus relative to the spin polarization of the atom:

$$\sigma_{N,F} \equiv \frac{\langle \mathbf{I} \cdot \mathbf{F} \rangle}{F(F+1)}. \quad (\text{B.4})$$

The next step is to relate $\sigma_{N,F}$ to the spin polarization of the valence proton $\sigma_{p,F}$ for a particular F . As discussed in Ref. [28], a reasonable estimate for K, Rb, and Cs nuclei can be obtained from the nuclear shell model by assuming that the nuclear spin \mathbf{I} is due to the orbital motion and intrinsic spin of only the valence nucleon and that the spin and orbital angular momenta of all other nucleons sum to zero. This is the assumption of the Schmidt or single-particle model [54]. In the Schmidt model, the nuclear spin \mathbf{I} is generated by a combination of the valence nucleon spin (\mathbf{S}_p) and the valence nucleon orbital angular momentum ℓ , so that we have

$$\begin{aligned} \sigma_{p,F} &= \frac{\langle \mathbf{S}_p \cdot \mathbf{I} \rangle}{I(I+1)} \sigma_{N,F}, \\ &= \frac{S_p(S_p+1) + I(I+1) - \ell(\ell+1)}{2I(I+1)} \sigma_{N,F}, \\ &= \sigma_p \sigma_{N,F}, \end{aligned} \quad (\text{B.5})$$

where it is assumed that the valence nucleon is in a well-defined state of ℓ and S_p , and σ_p is defined to be the fractional proton spin polarization for a given nucleus [28].

For comparison between GNOME magnetometers using different atomic species, it is essential to evaluate the uncertainty in the estimate of $\sigma_{p,F}$ based on the Schmidt model. To estimate this uncertainty, we compare calculations of $\sigma_{p,F}$ based on the Schmidt model to the results of the semi-empirical calculations described in Refs. [55, 56] and to the results of detailed nuclear shell-model calculations where available [57–59]. Conservatively, we assign the uncertainty in $\sigma_{p,F}$ to be given by the full range (maximum to minimum) of the values of $\sigma_{p,F}$ calculated by these various methods. It turns out that in each considered case, the estimate based on the Schmidt model gives the largest value of $|\sigma_{p,F}|$, causing the theoretical uncertainties in estimates of $\sigma_{p,F}$ to be one-sided as shown in Table II. Further details are discussed in Ref. [28].

2. SERF magnetometers

SERF magnetometers operate in a regime where the Larmor frequency is small compared to the spin-exchange rate, so that the rapid spin-exchange locks together the expectation values of the angular momentum projection $\langle M_F \rangle$ in both ground-state hyperfine levels of the alkali atom. Because the Landé g -factors g_F in the two ground-state hyperfine levels have nearly equal magnitudes but opposite signs, the magnitude of the effective Landé g -factor in a SERF magnetometer, $\langle g \rangle_{\text{hf}}$, is reduced compared to that in optical atomic magnetometers where a single ground-state hyperfine level is probed.

Table II. Fractional proton spin polarization $\sigma_{p,F}$, Landé g -factors g_F , and their ratios for the ground state hyperfine levels used in GNOME, and the weighted average of these values across both hyperfine levels ($\langle\sigma_p\rangle_{\text{hf}}/\langle g\rangle_{\text{hf}}$) applicable to SERF magnetometers in the low-spin-polarization limit. The estimates are based on the single-particle Schmidt model for nuclear spin [54] and the Russell-Saunders scheme for the atomic states. Uncertainties in the values for $\sigma_{p,F}$ describe the range of different results from calculations based on the Schmidt model, semi-empirical models [55, 56], and large-scale nuclear shell model calculations where available [57–59]. The uncertainties in $\sigma_{p,F}$ and $\langle\sigma_p\rangle_{\text{hf}}$ are one-sided because alternative methods to the Schmidt model generally predict smaller absolute values of the proton spin polarization. See Ref. [28] for further details.

Atom (state)	$\sigma_{p,F}$	g_F	$\sigma_{p,F}/g_F$	$\langle\sigma_p\rangle_{\text{hf}}/\langle g\rangle_{\text{hf}}$
$^{39}\text{K} (F = 2)$	$-0.15^{+0.06}_{-0.00}$	0.50	$-0.30^{+0.12}_{-0.00}$	$-0.5^{+0.2}_{-0.0}$
$^{39}\text{K} (F = 1)$	$-0.25^{+0.10}_{-0.00}$	-0.50	$0.50^{+0.00}_{-0.19}$	
$^{85}\text{Rb} (F = 3)$	$-0.12^{+0.02}_{-0.00}$	0.33	$-0.36^{+0.05}_{-0.00}$	$-0.8^{+0.1}_{-0.0}$
$^{85}\text{Rb} (F = 2)$	$-0.17^{+0.02}_{-0.00}$	-0.33	$0.50^{+0.00}_{-0.07}$	
$^{87}\text{Rb} (F = 2)$	$0.25^{+0.00}_{-0.05}$	0.50	$0.50^{+0.00}_{-0.11}$	$0.8^{+0.0}_{-0.2}$
$^{87}\text{Rb} (F = 1)$	$0.42^{+0.00}_{-0.09}$	-0.50	$-0.83^{+0.18}_{-0.00}$	
$^{133}\text{Cs} (F = 4)$	$-0.10^{+0.05}_{-0.00}$	0.25	$-0.39^{+0.19}_{-0.00}$	$-1.2^{+0.6}_{-0.0}$
$^{133}\text{Cs} (F = 3)$	$-0.13^{+0.06}_{-0.00}$	-0.25	$0.50^{+0.00}_{-0.24}$	

1219 To calculate the effective Landé g -factor averaged over
1220 hyperfine levels, $\langle g\rangle_{\text{hf}}$, for a SERF magnetometer, it is
1221 instructive to consider the equation describing the mag-
1222 netic torque on an alkali atom,

$$g_s \mu_B \mathbf{B} \times \langle \mathbf{S}_e \rangle \approx \frac{d\langle \mathbf{F} \rangle}{dt}, \quad (\text{B.6})$$

1223 where $g_s \approx 2$ is the electron g -factor and we have ig-
1224 nored the contribution of the nuclear magnetic moment.
1225 In the SERF regime, where the alkali vapor is in spin-
1226 exchange equilibrium, the populations of the Zeeman
1227 sublevels correspond to the spin-temperature distribu-
1228 tion [60] described by a density matrix in the Zeeman
1229 basis given by [61, 62]

$$\rho = C e^{\beta \cdot \mathbf{F}}, \quad (\text{B.7})$$

1230 where C is a normalization constant and β is the spin-
1231 temperature vector defined to point in the direction of
1232 the spin polarization P with magnitude

$$\beta = \ln \left(\frac{1+P}{1-P} \right). \quad (\text{B.8})$$

1233 In the low-spin-polarization limit,

$$\rho \approx C(1 + \beta \cdot \mathbf{F}). \quad (\text{B.9})$$

1234 It follows that

$$\langle \mathbf{S}_e \rangle = \text{Tr}(\rho \mathbf{S}_e) = \frac{1}{3} S_e (S_e + 1) \beta = \frac{1}{4} \beta, \quad (\text{B.10})$$

1235 and

$$\langle \mathbf{I} \rangle = \text{Tr}(\rho \mathbf{I}) = \frac{1}{3} I (I + 1) \beta. \quad (\text{B.11})$$

1236 Substituting the above expressions into Eq. (B.6) yields

$$\langle g \rangle_{\text{hf}} \mu_B \mathbf{B} \times \beta \approx \frac{d\beta}{dt}, \quad (\text{B.12})$$

1237 where

$$\langle g \rangle_{\text{hf}} = \frac{3g_s}{3 + 4I(I + 1)}. \quad (\text{B.13})$$

1238 Equation (B.13) can be compared to the g -factor for a
1239 particular alkali ground-state hyperfine level [63],

$$g_F = \pm \frac{g_s}{2I + 1}. \quad (\text{B.14})$$

1240 The effective proton spin polarization $\langle \sigma_p \rangle_{\text{hf}}$ for SERF
1241 magnetometers can also be derived by considering the
1242 relevant torque equation

$$\left(\frac{1}{f_{\text{int}}} \nabla a \right) \times \frac{\langle \mathbf{S}_p \rangle}{\|S_p\|} = \frac{d\langle \mathbf{F} \rangle}{dt}, \quad (\text{B.15})$$

$$\left(\frac{1}{f_{\text{int}}} \nabla a \right) \times \frac{\sigma_p}{\|S_p\|} \langle \mathbf{I} \rangle = \frac{d\langle \mathbf{F} \rangle}{dt},$$

1246 where we have used the fact that GNOME as configured
1247 for Science Run 2 is sensitive to the coupling of the ALP
1248 field to proton spins. In the low-spin-polarization limit,
1249 based on Eqs. (B.10) and (B.11),

$$\left(\frac{1}{f_{\text{int}}} \nabla a \right) \times \frac{\langle \sigma_p \rangle_{\text{hf}}}{\|S_p\|} \beta = \frac{d\beta}{dt}, \quad (\text{B.16})$$

1250 where

$$\langle \sigma_p \rangle_{\text{hf}} = \sigma_p \frac{4I(I + 1)}{3 + 4I(I + 1)}. \quad (\text{B.17})$$

Table II shows the ratio between the effective proton spin polarization averaged over both ground-state hyperfine levels, $\langle\sigma_p\rangle_{\text{hf}}$, to the effective Landé g -factor, $\langle g\rangle_{\text{hf}}$, in the low-spin-polarization regime. Note that the magnitudes of $\langle\sigma_p\rangle_{\text{hf}}/\langle g\rangle_{\text{hf}}$ are in general similar or slightly larger than the magnitudes of $\sigma_{p,F}/g_F$ for a single hyperfine level.

To determine the actual values of $\langle\sigma_p\rangle_{\text{hf}}/\langle g\rangle_{\text{hf}}$ for the SERF magnetometers used in GNOME's Science Run 2, more detailed considerations are required.

The values for the ratio of the effective proton spin polarization to the effective Landé g -factors for each GNOME magnetometer active during Science Run 2 are given in Table I.

a. Hefei magnetometer

The Hefei GNOME station employs a SERF magnetometer in a closed-loop, single-beam configuration, where the laser light is resonant with the Rb D1 line (pressure-broadened by 600 torr of nitrogen gas to a linewidth of ~ 10 GHz). The Hefei SERF magnetometer operates in the low-spin-polarization mode. The vapor cell contains ^{39}K , ^{85}Rb , and ^{87}Rb atoms in natural abundance, so spin-exchange collisions average over both ground-state hyperfine levels of all three species. Tak-

ing into account the relative abundances of the different atomic species at the cell temperature of $\approx 150^\circ\text{C}$ ($\approx 9\%$ ^{39}K , $\approx 65.5\%$ ^{85}Rb , $\approx 25.5\%$ ^{87}Rb), we find that $\langle g\rangle_{\text{hf}} \approx 0.193$, $\langle\sigma_p\rangle_{\text{hf}} = -0.073_{-0.000}^{+0.010}$, and thus $\langle\sigma_p\rangle_{\text{hf}}/\langle g\rangle_{\text{hf}} = -0.38_{-0.00}^{+0.05}$ for the Hefei magnetometer.

b. Lewisburg magnetometer

The Lewisburg GNOME station employs a SERF magnetometer in a closed-loop, two-beam configuration. The vapor cell contains only ^{87}Rb atoms. The Lewisburg SERF magnetometer operates with a spin-polarization $P \approx 0.5$, outside the low-spin-polarization regime. Discussions of the high-polarization regime are given in Refs. [62, 64]. For a nucleus with $I = 3/2$, the effective Landé g -factor is given by

$$\langle g\rangle_{\text{hf}} = g_s \frac{1 + P^2}{6 + 2P^2}, \quad (\text{B.18})$$

and the effective proton spin polarization is given by

$$\langle\sigma_p\rangle_{\text{hf}} = \sigma_p \frac{5 + P^2}{6 + 2P^2}. \quad (\text{B.19})$$

Based on Eqs. (B.18) and (B.19), we find that for the Lewisburg magnetometer $\langle\sigma_p\rangle_{\text{hf}}/\langle g\rangle_{\text{hf}} = 0.70_{-0.15}^{+0.00}$.

Figures

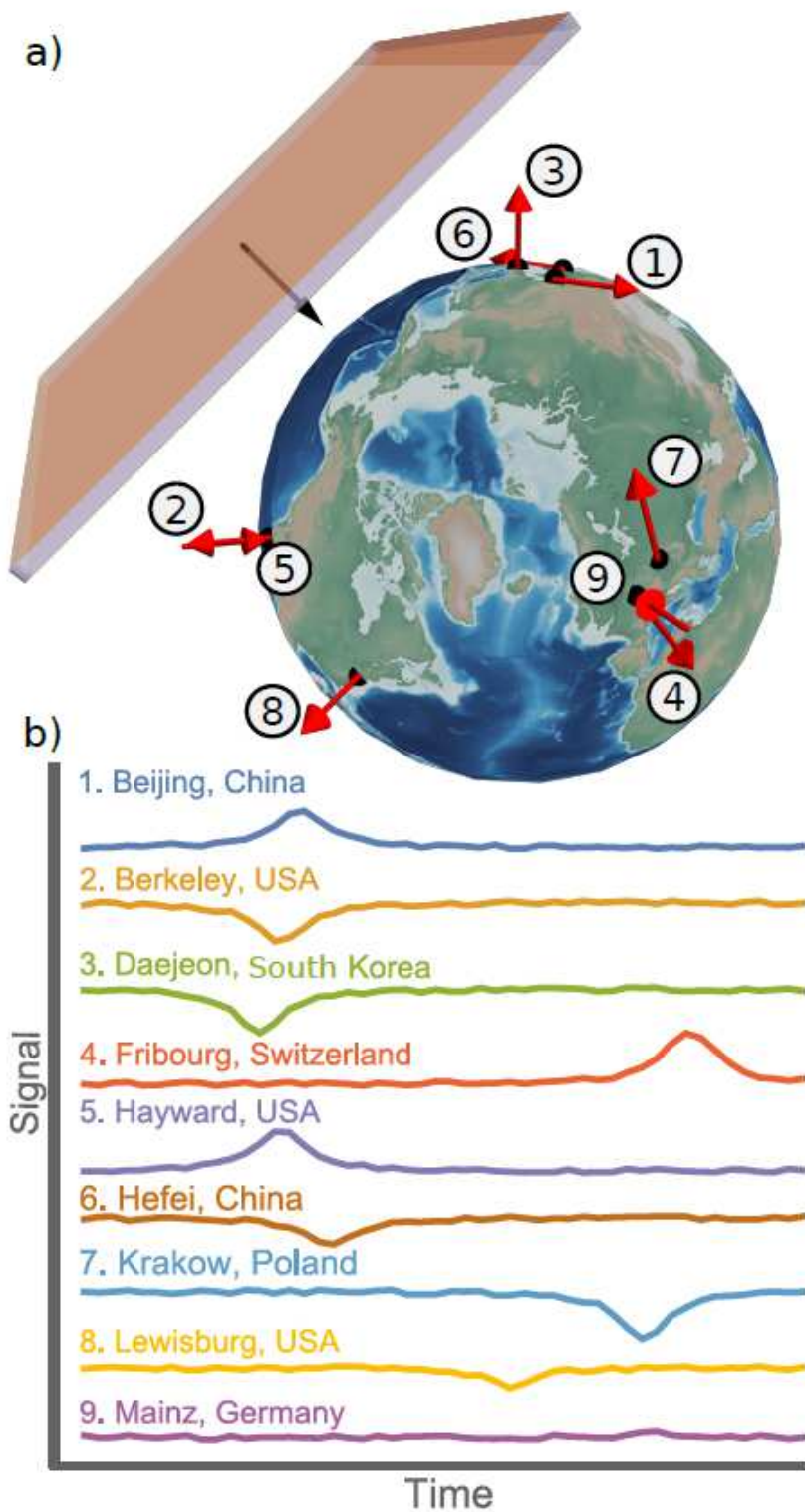


Figure 1

(a) Visualization of an ALP domain wall crossing the Earth. The red arrows indicate the position and sensitive axes of the GNOME magnetometers during Science Run 2 (Sec. I). (b) Simulation of the signals expected to be observed from a domain-wall crossing. Note: The designations employed and the

presentation of the material on this map do not imply the expression of any opinion whatsoever on the part of Research Square concerning the legal status of any country, territory, city or area or of its authorities, or concerning the delimitation of its frontiers or boundaries. This map has been provided by the authors.

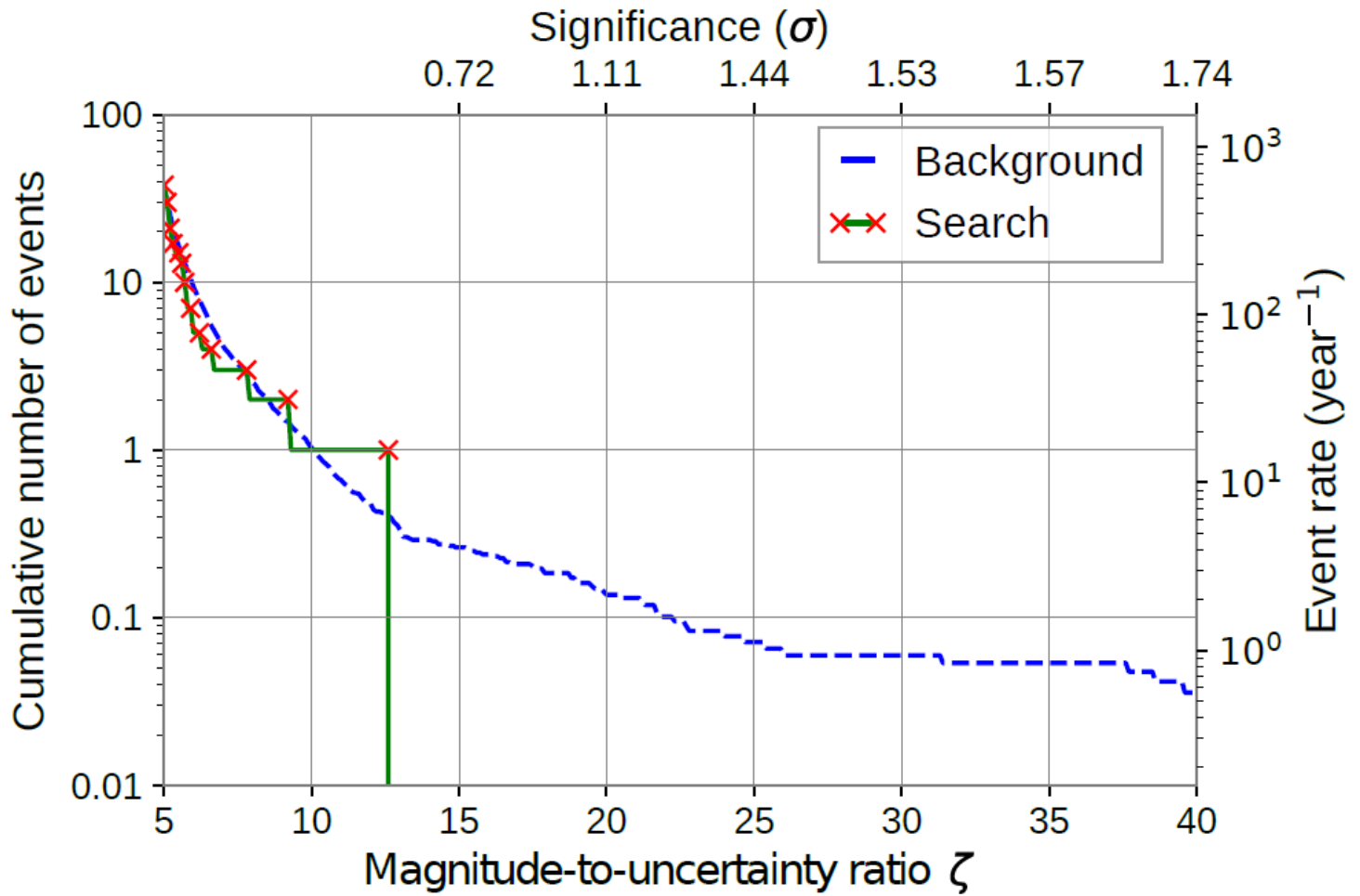


Figure 2

The blue dashed line represents the number events expected from the background in the twenty-three days of data from Science Run 2. 10.7 years of time-shuffled data are used to evaluate the background. The solid green line represents the number of events measured in Science Run 2. The red crosses indicate at which magnitude-to-uncertainty ratio new events are found. The upper axis indicates the statistical significance in units of Gaussian standard deviations of finding one event in the search data. The event with greatest magnitude-to-uncertainty ratio is found at 12.6.

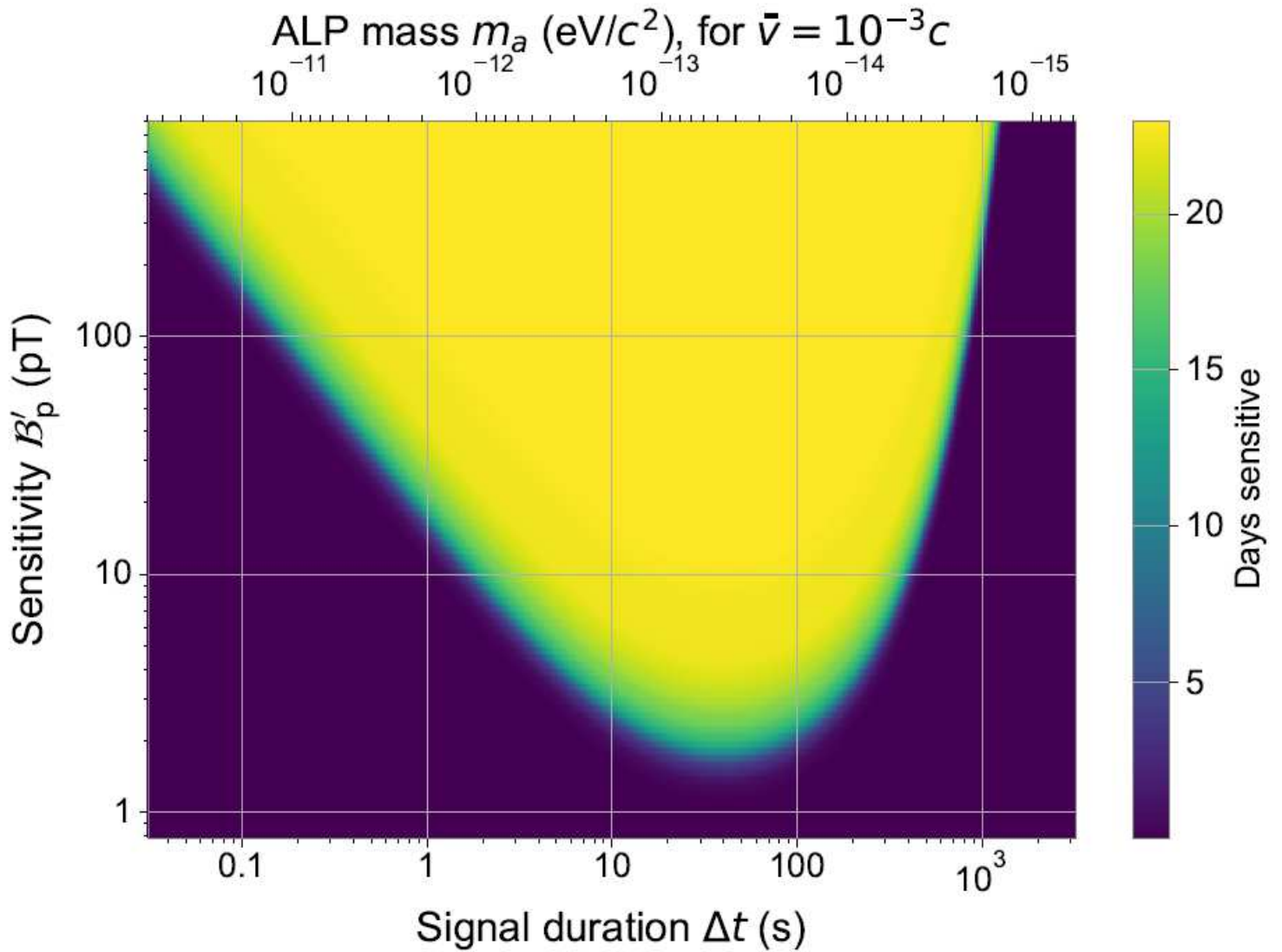


Figure 3

Amount of time T_{\sim} that the GNOME is sensitive to domain walls with a given duration Δt and normalized pseudo-magnetic field magnitude sensitivity B'_p throughout Science Run 2, the magnitude of an event needed to induce a signal with a magnitude-to-uncertainty ratio of one [see Eq. (11)]. Only the worst-case direction is considered. The plot assumes the parameters of the analysis: 20 s averaging time, 1.67 mHz first-order zero-phase Butterworth filter, and 50 Hz and 60 Hz zero-phase notch filters with a Q-factor of 60.

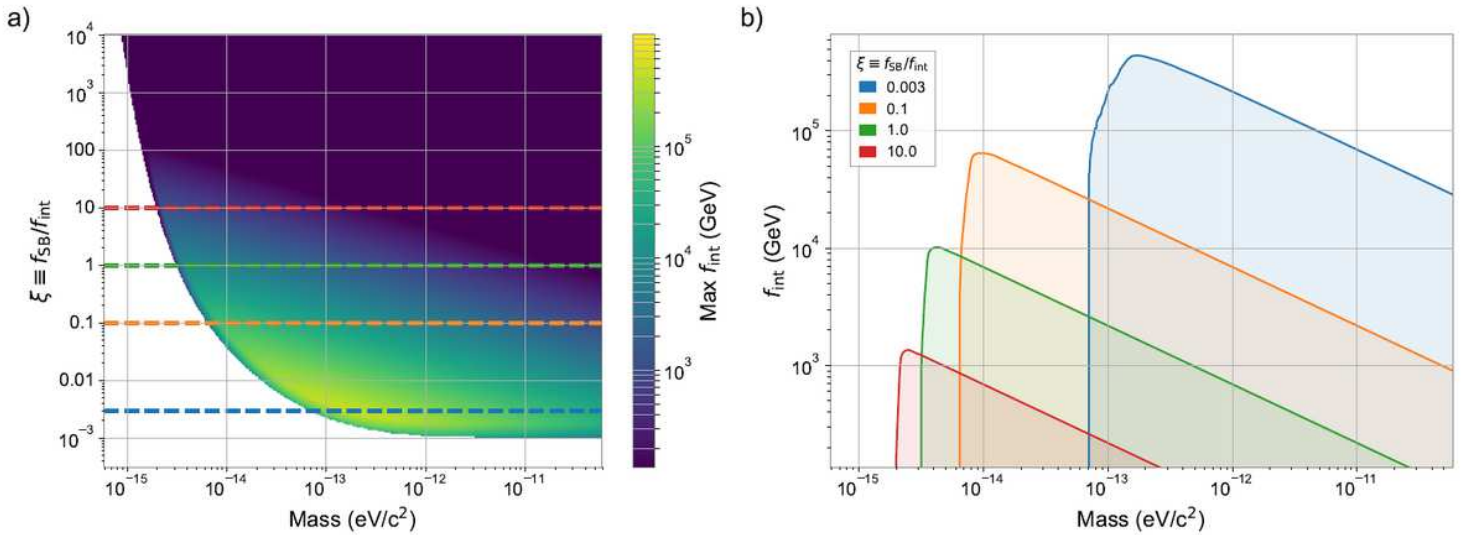


Figure 4

Parameter space of the ALP constrained by the presented analysis of Science Run 2 with 90% confidence level (see Sec. II). The relationship between ALP theory parameters and measured quantities are discussed in Sec. III and Appendix A. (a) In color, upper bound on the the interaction scale, f_{int} , to which the GNOME was sensitive as a function of m_a and the ratio $\xi \equiv f_{\text{SB}}/f_{\text{int}}$. (b) Cross-sections of the excluded parameter volume in (a) for different ratios ξ represented by the corresponding dashed lines of the matching color in (a).

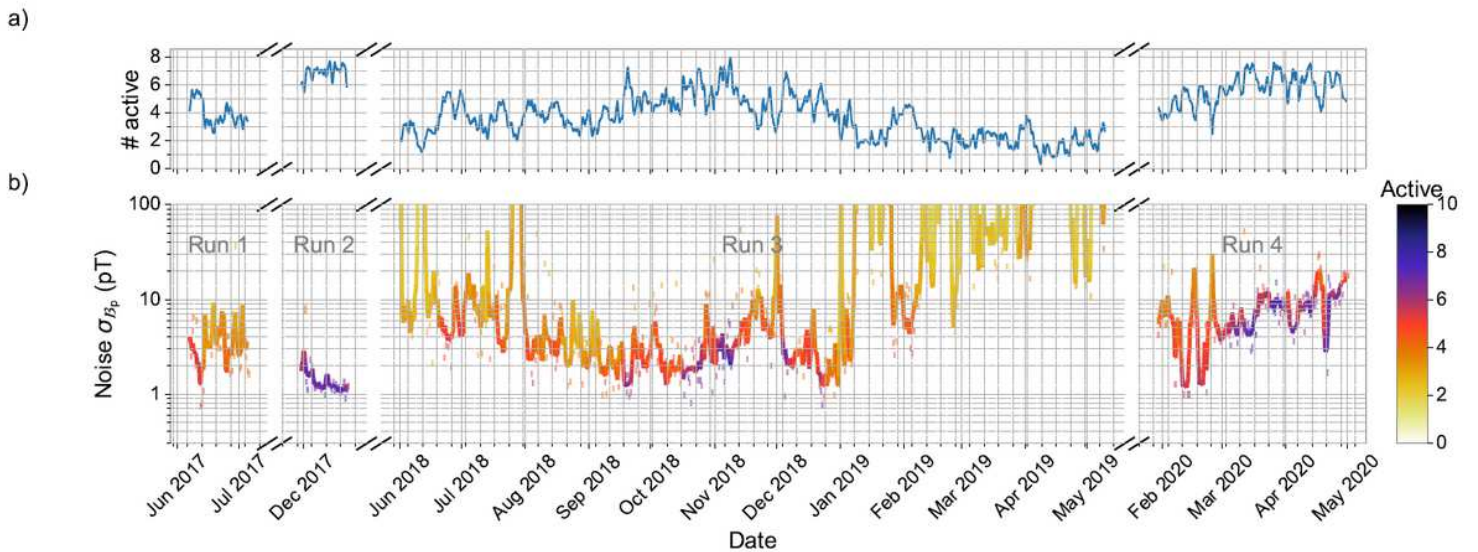


Figure 5

Summary of the GNOME performance during the four Science Runs from 2017 to 2020. The raw magnetometer data are averaged for 20 s and their standard deviation is calculated over a minimum of one and a maximum of two hours segments depending on the availability of continuous data segments. For each binned point, the combined network noise considering the worse case domain-wall crossing direction is evaluated as defined in Ref. [29]. (a) One-day rolling average of the number of active sensors.

(b) Multi-colored solid line represents the one-day rolling average of the combined network noise and the multi-colored dashes show the noise of the individual sampled segments. The data are preprocessed with the same filters used for the analysis. The number of magnetometers active is indicated by the color of the line and dashes.

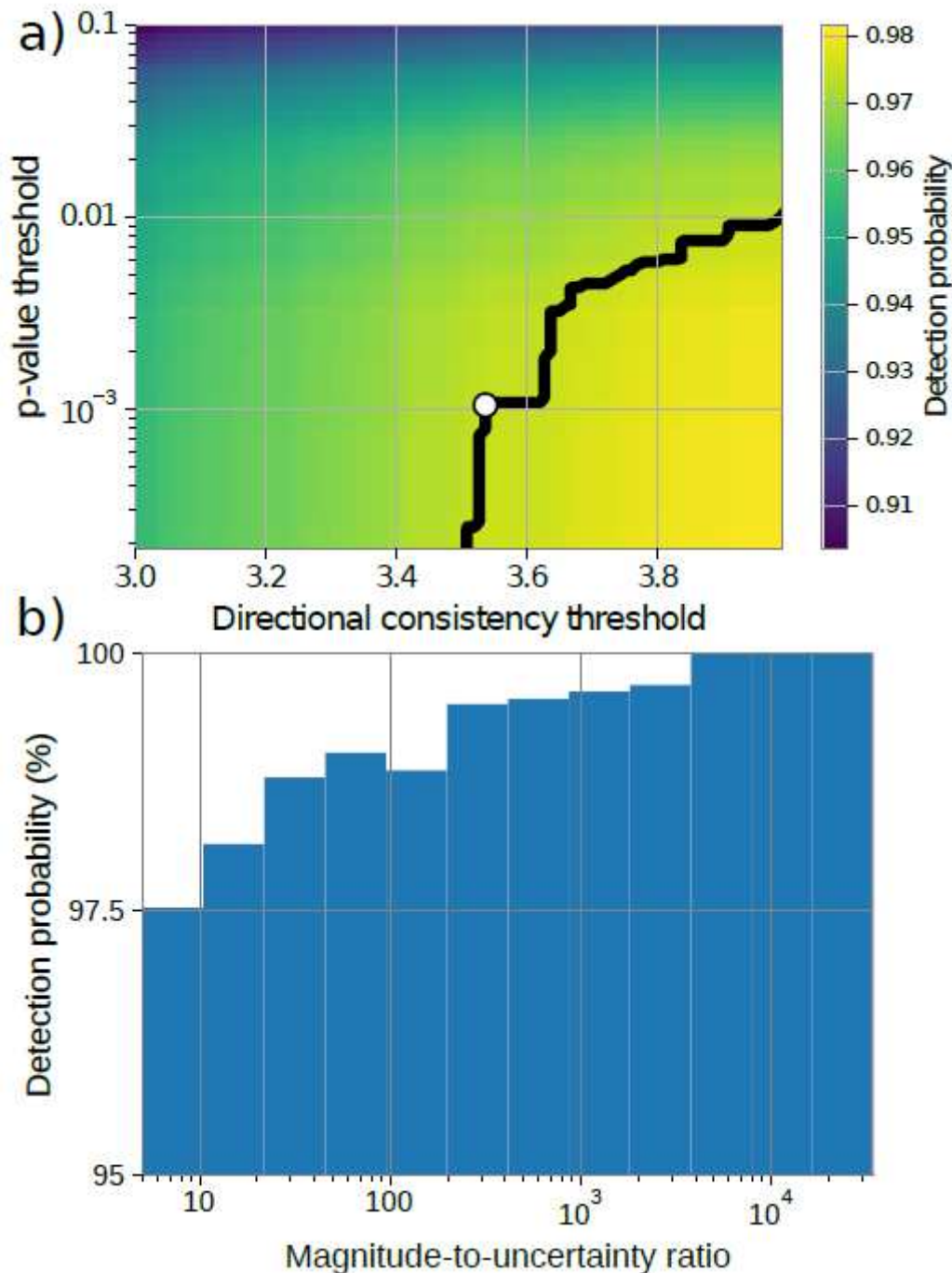


Figure 6

Summary of the true-positive analysis results. (a) shows the probability of detecting a domain-wall-crossing event with randomized parameters (as discussed in the text) as a function of p-value and directional-consistency thresholds. The inserted events have a magnitude-to-uncertainty ratio between 5

and 10. The black line indicates the combination of parameters corresponding to a 97.5% detection probability. The white dot indicates the particular thresholds chosen for the analysis. (b) Shows the mean detection probability reached for different magnitude-to-uncertainty ratios for the chosen thresholds.